Magnetically and thermally responsive nanoparticles for biomedical applications

By

Liliana Polo Corrales

A dissertation submitted in partial fulfillment of the requirements for the degree of

DOCTOR OF PHILOSOPHY

In

CHEMICAL ENGINEERING

UNIVERSITY OF PUERTO RICO

MAYAGÜEZ CAMPUS

2013

Approved by:

_____   _____
Carlos Rinaldi, Ph.D   Date
President, Graduate Committee

_____   _____
Madeline Torres Lugo, Ph.D   Date
Member, Graduate Committee

_____   _____
Eduardo Juan Garcia, Ph.D   Date
Member, Graduate Committee

_____   _____
Magda Latorre Esteves , Ph.D   Date
Member, Graduate Committee

_____   _____
Luis A. Rivera, Ph.D   Date
Representative of Graduated studies

_____   _____
Aldo Acevedo Rullan, Ph.D   Date
Chairperson of the Department

To God

To my whole family in Colombia

To my baby, the second heart that palpitated in my body

I love so much

Abstract

The synthesis of magnetic nanoparticles which respond to alternating magnetic fields by Brownian and Neel relaxation mechanisms are of great interest in determining mechanical properties of complex fluids in the size scale of the nanoparticles and in biomedical applications.   Because of their magnetic and thermal properties these particles are attractive in a wide range of applications including magnetic nanoparticle hyperthermia, which consists of destruction of cancer cells and tumors using the heat dissipated by magnetic nanoparticles in Alternating Magnetic Fields (AMFs).

In this work, it is demonstrated that the aging of iron-cobalt oleate complex promoted the formation of the spinel crystal structure which influenced the nanoparticle magnetic properties, resulting in an improvement of the magnetic properties. The applications of these magnetic nanoparticles allow the fabrication of nanoscale mechanical probes, which capitalize on the rotational response of the magnetic nanoparticles in an AMF and can be used to determine the nanoscale mechanical properties of a fluid.

In other applications, magnetic nanoparticles rotate or dissipate heat when acted upon by an alternating magnetic field (AMF). When coated with a thermoresponsive fluorescent polymer these can report changes in the local temperature. An important gap in this field is monitoring the local thermal effects at the magnetic nanoparticle surface under an alternating magnetic field (AMF). Theory indicates there should not

been higher temperature on the surface, but studies indicate that the heat dissipation of magnetic nanoparticles with Neel relaxation, affect the local environment surroundings.

.

Resumen

La síntesis de nanopartículas magnéticas que responden a campos magnéticos alternos por mecanismos de relajación browniano y Neel, son de gran interés en la determinación de las propiedades mecánicas de los fluidos complejos en la escala de tamaño de las nanopartículas y en aplicaciones biomédicas. Debido a sus propiedades magnéticas y térmicas estas partículas son atractivas en una amplia gama de aplicaciones, incluyendo hipertermia magnética, que consiste en la destrucción de las células cancerosas y los tumores utilizando el calor disipado por nanopartículas magnéticas en presencia de campos magnéticos alternantes.

En este trabajo, se demuestra que el añejamiento del complejo de oleato de hierro-cobalto promueve la formación de la estructura cristalina de espinela la cual influyó en las propiedades de las nanopartículas magnéticas, resultando en un mejoramiento de las propiedades magnéticas. Las aplicaciones de estas nanopartículas magnéticas permiten la fabricación de sondas mecánicas a nanoescala, que aprovechan la respuesta de rotación de las nanopartículas magnéticas en una campo magnético alterno. Además, puede ser utilizada para determinar las propiedades mecánicas a nanoescala de un fluido.

En otras aplicaciones, las nanopartículas magnéticas giran o disipan calor cuando actúan en presencia de un campo magnético alterno. Cuando ellas están

recubiertas con un polímero termosensible fluorescente pueden reportar cambios de la temperatura local. Una diferencia importante en este campo, es el monitoreo de los efectos locales termales en la superficie de nanopartículas magnéticas en presencia de un campo magnético alternante. La teoría indica que no debería haber una temperatura mayor en la superficie, pero los estudios indican que la disipación de calor de nanopartículas magnéticas con relajación Neel, afectan a los alrededores del entorno local.

Acknowledgments

I want to thank everyone who shared with me in this phase of my life, specially: I specially want to thank my advisor Dr. Carlos Rinaldi for his support and help.

My labmates and friends: Adriana Herrera, Edwin De La Cruz, Roberto Olayo, Veronica Sosa, Jeremiah Hubbard and Merlis Alvarez for help and friendship.

Joaquin Aparicio, Frances Roura, William Ortiz and Jennifer Olavarria for you friendship and support in difficult time in Puerto Rico.

Edwin De La Cruz and Roberto Olayo for help me with TEM measurements

Samuel Hernandez for help me and give facilities in his lab.

ABBOT Laboratories for give me fellowship during a period of my doctorate.

List of Contents

List of figures

List of Tables

1.   Introduction

Magnetic nanoparticles are interesting because they offer major advantages due to their size and physicochemical properties [1-5]. Among the ferrites most used are MFe_2O_4 (M: Co^{+2}, Fe^{+2}, Ni^{+2}, Mn^{+2}, etc.), which display attractive magnetic properties, making them useful for a wide range of applications such as in magnetic recording, catalysis, biotechnology, biomedicine, magnetic fluids, catalysis, magnetic resonance imaging, data storage, materials science, magnetic sensors, and magnetic separations [6-10] [11-13]. Also, their chemical and physical properties, superparamagnetism behavior, high field irreversibility, high saturation field, extra anisotropy contributions, and controlled size make then candidates for many applications[11-16].

The growing interest in obtaining cobalt ferrite nanoparticles with a narrow size distribution and that respond to changes in the magnetic field solely by the Brownian relaxation mechanism is motivated by applications such as magnetic nanosensors.

In this work, we study the effect of aging of the iron-cobalt oleate precursor on the nanoparticle's magnetic properties, such as blocking temperature and magnetocrystalline anisotropy constant.

Nanoscale magnetic materials have many advantages and opportunities in the biomedical field [17]. Examples of biomedical applications of magnetic nanoparticles are magnetic resonance imaging (MRI) [18], Magnetic fluid hyperthermia, manipulating cell membranes, targeted drug and gene delivery, and bionanosensors [19-22] In cancer

treatments, some of the challenges are localized transport, biocompatibility, stability in buffers, and low Curie temperature (Tc)[19, 20, 23] [24].

Magnetic Fluid Hyperthermia (MFH) is the localized increase of temperature ranging from 41 to 46 °C due to the energy dissipation caused by the particle response to the oscillating field. The induction of rotational motion of the magnetic dipoles causes energy dissipation. In cancer treatment, magnetic nanoparticles are transported to a cancer tumor in presence of a high frequency oscillating, resulting in cell death. However, some studies based on heat conduction theory have reported the local thermal effects of the magnetic nanoparticles in MFH do not present an advantage. We demonstrate through experiments that an immediate local thermal effect upon application of the alternating magnetic field occurs for a certain type of magnetic relaxation mechanism.

2. Objectives

2.1 General objective

Advance the application of magnetic nanoparticle based nanosensors in determining physical properties of fluids such as medium temperature and magnetic thermoresponsive properties of magnetic nanoparticles.

2.2 Specific objectives

- Study the Influence of aging time of oleate precursor on the magnetic relaxation of cobalt ferrite nanoparticles synthesized by the thermal decomposition method.

- Use the temperature sensitive fluorescence response of poly (N-isopropylacrylamide)-co-fluorophore and other acrylamide polymers to determine if application of an AMF (Alternating Magnetic Field) to magnetic nanoparticles indeed results in a localized temperature rise at the nanoparticle surface and elucidate the role of nanoparticle relaxation mechanism on such localized temperature rise.

3.   Background

3.1   Magnetic nanoparticle synthesis, characteristics and biomedical applications

The methods used to synthesize magnetic nanoparticles are classified as physical or chemical[12]. Some methods used to obtain shape-control and narrow size distribution are co-precipitation, microemulsion, hydrothermal synthesis, micelle synthesis, thermal decomposition, solvothermal, sonochemical, microwave assisted, chemical vapour deposition, combustion synthesis and laser pyrolysis synthesis[11, 13, 25, 26]. The size and size distribution of magnetic nanoparticles is typically determined by the chosen synthesis methodology.

3.1.1 Some methods for magnetic nanoparticles synthesis

Co-precipitation method: Offers an easy and economical route to synthesize magnetic nanoparticles. With this method, it is easy to prepare iron oxide nanoparticles from aqueous mixtures of ferric and ferrous chloride, in the presence of an ammonia hydroxide solution under an inert atmosphere and elevated temperature. Subsequently, the formed precipitate is separated by centrifugation or magnetic decantation. The type of salts used determines the size, shape, and composition of the magnetic nanoparticles[19, 20]. However, the nanoparticles possess a polydisperse size

distribution and formation of cluster-like aggregates is common[21-23]. The chemical reaction of formation may be written as[13]:

$$M^{2+} + 2Fe^{3+} + 8OH^- \rightarrow MFe_2O_4 + 4H_2O \qquad (3.1)$$

Where M can be Fe^{2+}, Mn^{2+}, Co^{2+}, Cu^{2+}, Mg^{2+}, Zn^{2+} and Ni^{2+}.

Thermal decomposition: Magnetic nanoparticles with high monodispersity, with narrow size distributions, good crystallinity, and smaller size can be synthesized using this method of high-temperature decomposition of organometallic compounds in high-boiling point organic solvents and in the presence of surfactants such as fatty acids, oleic acid and hexadecylamine for stabilization[24-27].

Microemulsion: This method consists in a thermodynamically stable isotropic dispersion of two immiscible liquids (water-in-oil microemulsions) stabilized by surfactant molecules. The molar ratio of water to surfactant determines the size of the reverse micelle which can be separated by the addition of solvents such as acetone or ethanol[11, 27].

Hydrothermal synthesis: is a synthesis method used for preparation of magnetic nanoparticles and ultrafine powders. The system consists of metal, ethanol based linoleate and a water–ethanol solution at different reaction temperatures under hydrothermal conditions. These reactions are performed in aqueous media in reactors

or autoclaves where the pressure can be higher than 2000 psi and temperatures higher than 200°C [11, 13, 25].

Sonochemical method: is a method used to prepare magnetic nanoparticles with unusual properties. During this process, temperatures of 5000K, pressures of 1800 atm and very fast cooling rates are produced which generate the formation of monodisperse nanoparticles[13, 25].

3.1.2 Ferrofluids

The ferrofluids are non-magnetic colloidal mixtures containing single-domain and permanently magnetized particles with a diameter between 15-20 nm. These colloidal mixtures are composed typically of water or oil and are used in various applications such as in nanoelectromechanical and microelectromechanical systems[28].

Ferrofluids are composed usually of ferrites such as magnetite, maghemite, cobalt ferrite, and others. Cobalt ferrite is of the most widely studied ferrites due to its room temperature coercivity, a blocking temperature and high magnetocrystalline anisotropy. This makes it attractive for high-capacity magnetic storage[29, 30], MRI contrast agents[7, 31], cancer thermotherapy[9, 31, 32], nanobiosensors based on the Brownian relaxation mechanism [33, 34], and nanoscale mechanical probes[35-39].

Ferrofluids are superparamagnetic at room temperature. Their magnetic behavior can be described through the Langevin function $L(\alpha)$[28]

$$L(\alpha) = \left(\coth \alpha - \frac{1}{\alpha} \right) = \frac{M}{M_s} \qquad (3.5)$$

where M is the magnetization of the ferrofluid, M_s is the saturation magnetization, and the parameter α represents the balance between the magnetic and thermal energy of the system, which can be written as[28]

$$\alpha = \frac{\pi \mu_0 M_d H d^3}{6kT} \qquad (3.6)$$

where H is the applied magnetic field, k is Boltzmann's constant (1.38×10^{-23} JK^{-1}), T is the temperature of the system, μ_0 is the permeability of free space ($4\pi \times 10^{-7}$ Hm^{-1}), M_d is the domain magnetization, and d is the diameter of the particle.

The response of a magnetic nanoparticle suspension to an oscillating magnetic field of small enough amplitude can be described by using the phenomenological magnetization relaxation equation in the absence of flow and particle rotation[40]

$$\frac{dM}{dt} = -\frac{1}{\tau}(M - \chi_0 H) \qquad (3.7)$$

Where *M* is the local magnetization vector of the suspension, τ is an effective magnetic relaxation time, χ_0 is the initial susceptibility of the suspension, and *H* is the applied magnetic field. Magnetic nanoparticles have two mechanisms for relaxation losses: Brownian and Néel[41, 42]. For Néel relaxation, the magnetic moment rotates from an easy axis toward the external field. For Brownian relaxation, the magnetic nanoparticles oscillate in the direction of the field and the magnetic moment is subject to mechanical friction due to the suspension medium. In magnetic fluid hyperthermia, magnetic nanoparticles with Néel relaxation are more desirable because they are not influenced by the local environment[43].

These relaxation times are typically modeled by[40]

$$\frac{1}{\tau} = \frac{1}{\tau_B} + \frac{1}{\tau_N} \ ; \ \ \tau_B = \frac{3V_h \eta_0}{kT}; \ \ \tau_N = \tau_0 exp\left(\frac{KV_m}{kT}\right) \tag{3.8}$$

Where V_h is the hydrodynamic volume of the particles, η_0 is the medium viscosity, *k* is Boltzmann's constant, *T* is the absolute temperature, τ_0 is a characteristic time, *K* is the magnetocrystalline anisotropy constant, and V_m is the volume of the magnetic core. It is commonly assumed that magnetic relaxation occurs through the faster of the two mechanisms (i.e., that with the shortest relaxation time).

Considering a sinusoidal variation in the applied magnetic field, $H = H_o \cos(\Omega t)$, the magnetization response is given by

$$M = \chi' H_0 cos(\Omega t) + \chi'' H_0 sin(\Omega t) \qquad (3.9)$$

,

Where Ω is the field frequency, and χ', χ'' are the real and imaginary components of the complex (dynamic) susceptibility $\hat{\chi}$.

When the magnetic nanoparticles are exposed to an oscillating magnetic field, it induces rotational motion, producing energy dissipation referred to as volumetric power dissipation (P)[44]. P is related to the increase in temperature with time of heating, known as the specific absorption rate (SAR). This energy dissipation is an important phenomenon which is based on the use of magnetic fluids for hyperthermia application. Both mechanisms are described by:

$$\boldsymbol{P} = \mu_0 \pi \chi_o f H_0^2 \left[2\pi f \tau / 1 + (2\pi f \tau)^2 \right] \qquad (3.10)$$

$$\boldsymbol{SAR} = \sum_i C_i m_i / m_{Fe} \ (dT | dt)_{\tau \to 0} \qquad (3.11)$$

3.1.3 Surface modification

For in vivo applications, the surface modification of magnetic nanoparticles is very important in order to make them biocompatible, non-toxic and stable to the reticulo-

endothelial system[45]. Nanoparticles with a hydrophobic surface are not stable in blood plasma and are easily removed from the circulation while hydrophilic particles can resist coating and are cleared much more slowly out of the body[46, 47].

Surfactants or polymers are used to disperse and keep in a stable colloidal state magnetic nanoparticles, avoiding agglomeration by electrostatic or steric repulsion[11]. Some polymers employed for this purpose are poly(ethyleneglycol), dextran, poly(lactic acid), chitosan, poly(pyrrole), poly(aniline), poly(alkylcyanoacrylates), poly(methylene malonate), polyesters, polyvinyl alcohol and their copolymers which contain functional groups such as carboxylic acids, phosphates and sulfates that bind to the surface of the magnetic nanoparticles[11, 47].

Polyethylene glycol (PEG): is a polymer used as a stabilizer because it is soluble in both polar and some non-polar solvents, is quite inert to chemical treatment and is biocompatible[48]. Therefore, it is used to modify magnetic surface providing an appropriate characteristic according to its application.
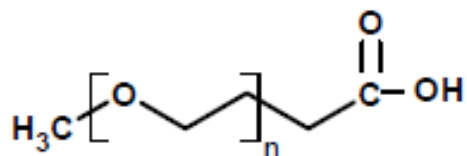
Figure 1.- Illustration of m-PEG-COOH polymer

In biomedical applications, PEG coating results in long circulation times, low toxicity, low immunogenicity, low clearance by the reticulo-endothelial system, non-degradability, heterogeneity, and accumulation of large linear PEG chains in the liver [49, 50].

Studies have demonstrated stability in colloidal dispersion of monodisperse magnetic nanoparticles with narrow size distribution and grafted with poly(ethylene glycol)-silane of different molecular weights in water[51-55], and these particles have been used in vitro studies to improve the biocompatibility of magnetic nanoparticles; such is the case of chitosan coated magnetic nanoparticles[56], PEG conjugated citrate-capped magnetite nanoparticles[57] and PEG-coated folic acid-modified superparamagnetic $MnFe_2O_4$ nanoparticles[58]. Also, it has been used in bio-applications such as cell isolation, immunoassays, enzyme immobilization, drug delivery, and protein separation[59-62].

Lately, the use of PEG coated magnetic nanoparticles with long-circulating times in vivo studies employing a rat model to explore the biodistribution patterns of PEG coated magnetic nanoparticles (liver, spleen, lung, and kidney) has been reported [63, 64]. Also, it has been employed as covering of magnetic nanoparticles for effective MRI contrast agents for cancer diagnosis[65]. Other applications using PEG as the coating are related with the synthesis of ferrofluids based on superparamagnetic particles in dispersion to prevent aggregation or magnetostatic interactions and provide excellent thermal stability and a large useful temperature range[66].

The characterization of the rheological properties of the ferrofluids plays an important role in the molecular design/application of magnetorheological fluids because the rheological properties of the fluids, such as the apparent viscosity, yield stress, and stiffness, can be controlled by an external magnetic field [67]. Also, it has been used to obtain information about the mechanical properties of complex fluids and physical parameters such as melting points and gelation temperatures[37].

Thermoresponsive fluorescent polymers based on poly-N-isopropyl acrylamide (PNIPAM) and benzofurazan monomers.

Thermosensitive polymers have been extensively studied for their application in drug delivery, gene therapy, bioconjugation, enzyme immobilization, protein dehydration, and thermal affinity separation [68-70]. Polymers such as poly (N-isopropylacrylamide), exhibit a lower critical solution temperature (LCST) above which their solubility in water decreases, resulting in phase separation [71-73]. At the LCST, the enthalpy of water hydrogen bonded to amide groups of the pNIPAM chain decreases, resulting in loss of bound water to the bulk solution[72, 73]. In drug delivery, pNIPAM chains are swollen at a temperature below the LCST in an aqueous solution which contains a drug or cargo and when the temperature increase above the LCST the contraction of the hydrogel structure expels the drug.

N-isopropylacrylamide has been used to obtain non-invasive molecular thermometers by combining with fluorophores and chromophores incorporated in the polymer chains to monitor the LCST[69, 74].
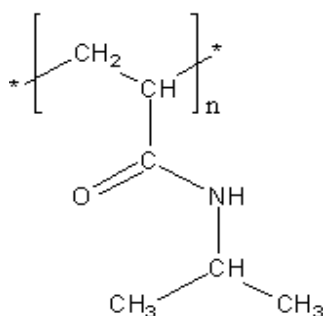
Figure 2.- N-isopropylacrylamide (p-NIPAM) polymer

DBD-AE (a benzofurazan type fluorphore) is one fluorophore with fluorescence intensity that increases with decreasing solvent polarity as the pNIPAM is heated[75, 76].
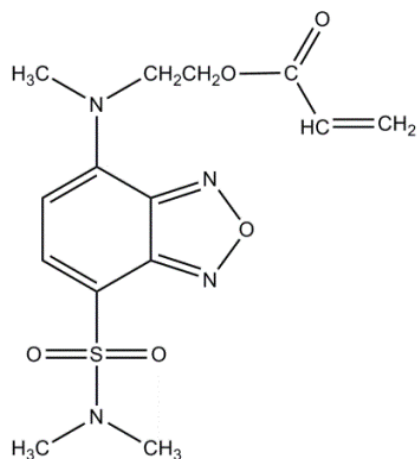
Figure 3.- A benzofurazan type fluorphore

Herrera et al synthetized IO (Iron Oxide) nanoparticles coated with fluorescent thermo-responsive polymeric shells of poly(N-isopropylacrylamide-Fluorescent Modified Acrylamide) p(NIPAM-co-FMA) for potential use with magnetic fields where the rotational motion causes energy dissipation and a localized increase in temperature, changing the structure of the surrounding polymer[74].

3.1.4 Biomedical applications using magnetic nanoparticles.

Biomedical applications of magnetic nanoparticles are classified as in *vivo* and in *vitro*. The principal in vitro applications are magnetorelaxometry, diagnostic separation processes, and selection whereas for in vivo applications, they include therapeutic and diagnostic applications[5]. Two key factors play an important role for in vivo applications: size and surface functionality. Particles with diameters of 10-40 nm are optimal for prolonged blood circulation in capillaries, lymph nodes, and bone marrow [13].

In vitro applications

Separation and selection: In this application the magnetic adsorbent is added to a solution which contains a target to absorb. Later, the adsorbed target is recovered from the suspension using an appropriate magnetic separator[5]

Magnetorelaxometry: is a technique based on the measurements of the magnetization of a sample with embedded superparamagnetic nanoparticles after aligning the magnetic moments and the detection of their relaxing magnetization following switching-off the magnetic field. The response of the sample can change by means of two mechanisms Neel relaxation and Brownian relaxation.

Magnetic resonance imaging: This technique is noninvasive and allow for real-time detection of diseases such as cancer and give information about its stages[77]. Superparamagnetic and paramagnetic nanoparticles are used as contrast agent by shortening the T2 relaxation time of protons located nearby. The principal paramagnetic ions used as T2 contrast agents in MRI applications are manganese (Mn), chromium (Cr), and gadolinium (Gd) and Superparamagnetic iron oxide (SPIO)[5, 77, 78].

Bioseparation: This technique refers to the separation of specific biological entities such as DNA, proteins and cells from their environment in order to be analyzed. These superparamagnetic nanoparticles are used for the transportation of biomaterial in the presence of a magnetic field[5, 79].

In vivo applications

Hyperthermia: Is a thermal treatment used in cancer therapy based on different types of methods (hot water, capacitive heating and inductive heating of malignant cells) [80]. The cancerous cells are vulnerable to a range of temperature between 42-46°C

and reduce their viability while normal cells can survive at this condition. This technique is promising for cancer treatment because of the ease in targeting the cancerous tissue and hence having fewer side effects than chemotherapy and radiotherapy[5]. The use of magnetic nanoparticles has increased in biomedical applications, because they can be transported to a target tissue and then apply an AC magnetic field of sufficient strength and frequency to produce heat into immediately surrounding diseased tissue destroying the cancer cells to temperatures of 40-46°C[80].

Drug delivery: Magnetic nanoparticles are being used as drug carriers due to tailored drug release characteristics, yielding improved treatment efficacy and reduction of unwanted side effects and low immunogenicity[81]. The delivery occurs by external stimuli such as electric current, magnetic fields, temperature, light and ultrasound[24]. Drug localization using magnetic delivery systems refers to the competition between the forces exerted on the particles in the blood and the magnetic forces produced from the magnet[5]. The magnetic nanoparticles used in drug delivery applications require a physicochemical and targeting design to be capable of carrying and protecting the loaded drug, cellular drug resistance and an optimal mechanism of release[82].

3.2 Magnetic nanoparticles for hyperthermia and triggered release

Magnetic fluid hyperthermia is a promising alternative cancer treatment wherein magnetic nanoparticles are targeted to cancer cells or tissues where they dissipate heat. This process consists in the transport of magnetic nanoparticles to a solid tumor under a magnetic field (10 kA/m and high frequencies) making the particles dissipate

heat [83]. The dissipated energy is transferred to the tissue or tumor and causes apoptosis of cells or cell death.

Magnetic nanoparticles with the Néel relaxation raise the temperature above 43 °C causing cell death [84]. Also, larger particles are used for triggered drug release due to the fact that they respond to an alternating magnetic field showing Brownian relaxation[85].

Magnetic Fluid Hyperthermia has certain advantages on the traditional hyperthermia. Some advantages are shown in **Table. 3.1**[86]

Table 1.-Traditional hyperthermia vs. Magnetic Fluid Hyperthermia

Traditional hyperthermia	Magnetic Fluid Hyperthermia
➤ Uses external devices to transfer energy to tissues(irradiation with light)	➤ Uses oscillating magnetic fields to dissipate thermal energy to the tissues.
➤ Techniques used for induction of heat are ultrasound, radiofrequency, microwaves, infrared radiation and tubes with hot water.	➤ The frequencies of oscillating magnetic fields cause heat dissipation in magnetic nanoparticles.
➤ Causes heating of healthy tissue producing burns, blisters and discomfort.	➤ Magnetic nanoparticles can be targeted to a specific site in the body using cancer-specific binding agents.
➤ Uses macroscopic implant.	➤ Uses magnetic particles with size at nanoscale which allows easy passage into several tumors.

3.3 Magnetic nanoparticle as nanoscale mechanical probes

The use of Magnetic nanoparticles as mechanical nanoprobes[87] are a novel strategy used to study the interactions and dynamics of network formation in structured materials,[37] and   as biosensors for specific binding of a targeted analyte. Such biosensors work by detecting   changes in the hydrodynamic radius and Brownian relaxation time[88].

There are nanoprobes that combine fluorescent and reflection detection for the study of viscous drag and torque on the scale of microns to tens of nanometers [89] However, fluorescent probes require careful separation methods to eliminate background fluorescence which affects the sensitivity with respect to location and time[90].

Researchers have confined magnetic nanoparticles which can be manipulated at the intracellular level inside endosomes and vesicles by monitoring the rotation of aggregated chains one can obtain information on the viscoelastic properties of their microenvironment[91].

A novel methodology for the detection of binding of biomolecules to colloidal magnetic particles in suspension through AC magnetic susceptibility measurements was proposed for Connolly and St Pierre[92]. This method is based on bulk rotation of the nanoparticle within the fluid, with Brownian rotational diffusion time τ_B [92]

The Debye model, derived to analyze dielectric dispersion in dipolar fluids, can be used to describe the response of the magnetization of a dilute suspension of spherical magnetic particles to an alternating magnetic field[92] when the dipole-dipole interaction energy is smaller than the thermal energy *kT* and the complex susceptibility of the magnetic fluid has the frequency dependence $\chi(\omega)$[93]

$$\chi(\omega) = \chi_\infty + \frac{\chi_0 - \chi_\infty}{1 + i\omega\tau} \qquad (3.12)$$

Where

$$\tau = \frac{1}{\omega_{max}} = \frac{1}{2\pi f_{max}} \qquad (3.13)$$

And

$$\chi'(\omega) = \frac{\chi_0}{1 + (\omega\tau)^2)} \; , \; \chi''(\omega) = \frac{\chi_0 \omega\tau}{1 + (\omega\tau)^2} \qquad (3.14)$$

Here f_{max} is the frequency where $\chi(\omega)$ reaches its maximum value, χ_0 is the static susceptibility value; $\chi(\infty)$ is the susceptibility at high frequency, $\chi'(\omega)$ is the real component and $\chi''(\omega)$ is the imaginary component. The maximum value for $\chi''(\omega)$ at $\omega\tau=1$ provides information on the relaxation time of the magnetic nanoparticle.

Experimental studies have demonstrated the detection of biomolecules such as proteins[94] and antibodies[95, 96], using magnetic nanoparticles in buffers. These methods are based on the change of hydrodynamic radius due to the binding reaction

with the magnetic nanoparticle, and the increase in hydrodynamic radius induces a decrease in $\chi''(\omega)$.

Studies in this area contribute to the advance of magnetic nanoparticles based sensors to determine properties of fluids such as medium temperature, local viscosity, and to sense the presence of a chemical species of interest.

4 Influence of Aging Time of Oleate Precursor on the Magnetic Relaxation of Cobalt Ferrite Nanoparticles Synthesized by the Thermal Decomposition Method

We studied the influence of aging time of the iron-cobalt oleate precursor on the structure, chemical composition, size, and magnetic relaxation of cobalt ferrite nanoparticles synthesized by the thermal decomposition method. The structure and thermal behavior of the iron-cobalt oleate was studied during the aging process. Infrared spectra indicated a shift in the coordination state of the oleate and iron/cobalt ions from bidentate to bridging coordination. Aging seemed to influence the thermal decomposition of the iron-cobalt oleate as determined from thermogravimmetric analysis and differential scanning calorimetry, where shifts in the temperatures corresponding to decomposition events and a narrowing of the endotherms associated with these events were observed. Aging promoted formation of the spinel crystal structure, as determined from X-ray diffraction, and influenced the nanoparticle magnetic properties, resulting in an increase in blocking temperature and magnetocrystalline anisotropy. Mossbauer spectra also indicated changes in the magnetic properties resulting from aging of the precursor oleate. Although all samples exhibited some degree of Brownian relaxation, as determined from complex susceptibility measurements in a liquid medium, aging of the iron-cobalt oleate

precursor resulted in crossing of the in-phase χ' and out-of-phase χ'' components of the complex susceptibility at the frequency of the Brownian magnetic relaxation peak, as expected for nanoparticles that relax through a single relaxation mechanism. The resulting nanoparticles would be suitable for sensors based on the Brownian relaxation mechanism and in determining mechanical properties of complex fluids at the size scale of the nanoparticles

Previous work

Bao and coworkers studied the formation mechanism and shape control of cobalt ferrite nanoparticles obtained from the thermal decomposition of iron/cobalt oleates[97, 98]. They evaluated the structure of the iron-cobalt oleate complex, concluding that three oleate ligands bind to the Fe^{+3} ion and two oleate ligands bind to the Co^{+2} ion. The formation mechanism of cobalt ferrite nanoparticles was then related to the temperature at which each metal oleate decomposes, leading to homogeneous nucleation. This temperature was determined to be in the range of 300-314 °C. Furthermore, time dependence of nanoparticle growth was studied at 320 °C, observing a direct relationship between size, nanoparticle shape, and reaction time. Additionally, they observed that the shape of the synthesized nanoparticles did not affect their saturation magnetization, but the coercivity exhibited a small shape dependence, which was attributed to the influence of surface anisotropy. Unfortunately, the magnetic relaxation mechanism of the synthesized cobalt ferrite nanoparticles was not determined. To the best of our knowledge, the effect of aging time of the iron-cobalt oleate precursor on its

structure and thermal behavior has not been studied. Furthermore, how the aging time of this oleate precursor influences the structure, chemical composition, size, and magnetic relaxation of the synthesized cobalt ferrite nanoparticles obtained by the thermal decomposition method is unknown.

We were interested in obtaining cobalt ferrite nanoparticles with a narrow size distribution and that respond to changes in the magnetic field solely by the Brownian relaxation mechanism. After a series of syntheses, we observed that some samples had better Brownian response than others, based on frequency dependent AC susceptibility measurements; and that such samples typically corresponded to syntheses where some time had passed after oleate precursor preparation. This led us to hypothesize that aging of the oleate precursor may be occurring and influencing the properties of the resulting nanoparticles.

Thus we were motivated to carry out a study to compare samples of cobalt ferrite nanoparticles synthesized using iron-cobalt oleates aged in the dark at room temperature for up to 30 days. In this paper we present the results of this study, showing that aging affects the thermal decomposition of the iron-cobalt oleate precursor, promoting the formation of the correct ferrite crystal structure, as observed through X-ray diffraction measurements.

Furthermore, aging of the iron-cobalt oleate precursor influenced the nanoparticle's magnetic properties, such as blocking temperature and magnetocrystalline anisotropy

constant. We compared the relaxation times of the synthesized cobalt ferrite nanoparticles and, although all samples exhibit some degree of Brownian relaxation, aging of the iron-cobalt oleate precursor influenced their AC susceptibility spectra, resulting in crossing of the in-phase χ' and out-of-phase component χ'' of the complex susceptibility at the peak of the χ'' curve, an attribute of nanoparticles with a single relaxation mechanism.

4.1 Experimental section

Materials

Metals: iron (III) chloride hexahydrate 97% Sigma Aldrich and cobalt (II) hexahydrate 98% Aldrich.

Surfactants: sodium oleate reagent grade from Tokyo Chemical Industry.

Organic solvents: 1-octadecene reagent grade from Tokyo Chemical Industry, ethanol, hexane and acetone from Fluka.

Synthesis procedure

An iron-cobalt oleate precursor was prepared by reacting 32 g (120 mmol) of iron (III) chloride hexahydrate, 14 g (60 mmol) of cobalt (II) chloride hexahydrate, and 146 g (480 mmol) of sodium oleate at 70 °C in 1.2 L of a mixture of water (300 ml), ethanol (300 ml), and hexane (600 ml) for 4 h using a reflux condenser [1]. Afterwards, the reaction

mixture was cooled to room temperature and the aqueous phase was decanted using a separation funnel. The iron-cobalt oleate solution was washed three times with distilled water (300 ml) using a separation funnel and transferred to a vacuum oven at 80 °C for 48 h to evaporate the organic solvents and water, obtaining a viscous liquid with a dark reddish appearance. Afterwards, the dry iron-cobalt oleate precursor was aged in the dark at room temperature for a period of up to 30 days.

Cobalt ferrite nanoparticles were synthesized by the thermal decomposition method using 1-octadecene as solvent [99, 100]. The iron-cobalt oleate precursor was used at different aging times of 2, 14, and 30 days, to obtain cobalt ferrite nanoparticles which were labeled as 2D, 14D, and 30D, respectively. In a typical synthesis, 25 g of the aged iron-cobalt oleate were mixed with 100 ml of 1-octadecene and 2 g of oleic acid. This reaction mixture was stirred at room temperature for one hour with bubbling nitrogen. Then, temperature was increased to 320 °C at a heating rate of 3.5 °C/min. Bubbling nitrogen was stopped when the temperature reached 200 °C. Reaction was carried out at 320 °C for 3 h. Afterwards, the reaction mixture was cooled to room temperature. Nanoparticles were obtained by washing with acetone (1:3 volume ratio) and centrifuging at 8000 rpm for 15 min. This procedure was repeated three times.

4.2 Characterization

A Varian 800 FTIR and ZnSe attenuated total reflection (ATR) holder with a wavenumber range of 4,000–600 cm^{-1} was used to characterize the iron-cobalt oleate. The thermal decomposition behavior of the aged iron-cobalt oleate was studied as a function of aging time by thermogravimetric analysis using a TA-2950 Thermo Gravimetric Analyzer.   The weight loss percentage was recorded in the temperature range of 50 to 450 °C with a heating rate of 3.5 °C/min using air at 60 ml/min. Differential scanning calorimeter was performed using a TA Instruments Q2000 DSC in the temperature range of 50 to 450 °C with a heating rate of 20 °C/min using nitrogen at 50 ml/min.

The size and size distribution of the synthesized magnetic nanoparticles were determined by Transmission Electron Microscopy (TEM) using a Zeiss LEO 922 operating at 200 kV.   For these measurements, ultra-thin carbon type A grids were immersed in samples of nanoparticles suspended in hexane, which were then placed on filter paper and dried in a vacuum oven. The hydrodynamic diameter of the synthesized nanoparticles was measured using a Brookhaven Instruments BI-90 Plus particle size analyzer.   Samples of the nanoparticles were suspended in hexane and then filtered with 0.1 μm PTFE filter syringes prior to analysis.

X-Ray powder diffraction was used to determine crystal size and structure of dry powder samples of nanoparticles using a Siemens B500 DACO-MP Diffractometer equipped with a Cu K_α radiation source (40 kV, 44 mA; λ = 1.54 Å). Data were obtained

from 2θ angles of 2-80° at a scan rate of 0.03°/s. To obtain dry powder samples, nanoparticles were washed with a reflux of acetone at 70 °C to remove the oleic acid surfactant. Inductively coupled plasma optical emission spectrometry (ICP-OES) was used to determine the incorporation of cobalt and iron in the nanoparticles. A Perkin Elmers Optima 2000 DV instrument was used for these measurements. Dry powder samples of magnetic nanoparticles were digested in nitric acid (12 M) at 100 °C overnight. Afterwards, they were diluted with deionized water to obtain a concentration of 2 % v/v HNO_3. Calibration curves of iron and cobalt absorption standards were used to determine sample composition.

Mössbauer spectra of powder samples were recorded at room temperature using a SEECo MS4 Mössbauer Spectrometer, at constant acceleration mode, with a 50mCi ^{57}Co source in Rh-matrix. The calibration was carried out with a 25µm thick α-Fe absorber. Spectral analyses were carried out with WMOSS software, using the hyperfine distribution model according to Rancourt and Ping [101].

Magnetic properties were determined using a Quantum Design MPMS XL-7 SQUID magnetometer. To report the magnetic properties of the synthesized nanoparticles, measurements were normalized by the mass of inorganic core in the samples, which was determined from TGA by assuming the remnant mass after decomposition of the sample at 800°C corresponds to the inorganic cores. The magnetic core size and saturation magnetization of magnetic nanoparticles suspended in hexane at 10 % w/w were determined by measuring the response of the equilibrium magnetization under the

application of a DC magnetic field. The coercivity of the magnetic nanoparticles was determined at 2, 300, and 400 K by immobilizing the synthesized nanoparticles in a solid matrix of poly(styrene-divinylbencene) at 1 % w/w[102]. For this measurement, nanoparticles were suspended in a solution of styrene with 15 % v/v of DVB and 0.37 % w/w of AIBN and sonicated for 5 min. The reaction mixture was heated to 70 °C at a heating rate of 10 °C/h using an ethylene glycol bath. Polymerization was carried out for 3 h. The blocking temperature of nanoparticles immobilized in PSDVB matrix was obtained from the temperature dependence of the magnetization under zero-field-cooled (ZFC) and field-cooled (FC) conditions at 1 mT. To study the magnetic relaxation of the synthesized nanoparticles, AC susceptibility measurements were performed as a function of the applied field frequency for nanoparticles suspended in mineral oil (10 %w/w) at 273 K.

4.3 Results

Iron-cobalt oleate

FTIR: The precursor iron-cobalt oleate was analyzed by FTIR at various times during the aging process which is showed in the **Figure 4**. In the **Figure 4.a)** is showed the spectra for iron-cobalt oleates at 2 days and 30 days and for iron and cobalt oleates. Characteristic vibrational bands were observed at 2920 and 2853 cm^{-1}, which can be attributed to the stretching –CH$_2$ vibration; 1700 cm^{-1}, related to the C=O stretch of carboxylic acids; 1595 cm^{-1}, attributed to the asymmetric ν_{as} stretch of COO$^-$

carboxylates; 1408 cm^{-1}, related to the symmetric ν_s stretch of COO$^-$ carboxylates; and 720 cm^{-1}, identified with the O−C=O bend of carboxylic acids [3, 4, 6, 7]. The presence of bands at 1700 and 720 cm^{-1} indicates that some oleic acid was formed during the synthesis process and that it remains in the iron-cobalt oleate. No changes were observed with time for iron and cobalt oleate whereas for iron-cobalt oleate such changes were done.

Moreover, significant differences were observed between the spectra for the iron, cobalt, and iron-cobalt oleates. **Figure 4.b)** shows spectra in a region of interest between 1800 and 1200 cm^{-1} for an iron-cobalt oleate aged over a period of 30 days. Here it is seen that the relative contributions of two peaks between 1600 and 1500 cm^{-1} change over the course of the experiment. The spectra in this range consists of two primary contributions: a peak around 1595 cm^{-1} corresponding to band splitting due to a bridging coordination between oleate and metal ions and a peak around 1555 cm^{-1} corresponding to band splitting due to bidentate coordination of an oleate and two metal ions. As the oleate ages we observe the relative contributions of these two peaks change, with the peak corresponding to bidentate coordination decreasing in magnitude relative to the peak corresponding to bridging coordination. This is illustrated in **Figure 4.c)** by plotting the ratio of the absorbance at 1555 cm^{-1} with respect to the absorbance at 1595 cm^{-1}, where it can be seen that at first this ratio decreases rapidly and then it plateaus after about 10 days.

Thermogravimetric Analysis: The thermal decomposition behavior of the aged iron-cobalt oleate was studied as a function of aging time by thermogravimetric analysis. TGA data plotted as weight percentage as a function of temperature (**see Appendix A1**). We found that the mass remaining at the end of the TGA run changed with aging, from 11.2% at 2D to 7.82% at 14D, to 7.7% at 30D. We believe the difference between 2D and 14D/30D may be significant, but the difference between 14D and 30D is below experimental error. We also considered the total weight loss observed in the first step of the ramp and found that for 2D there was a weight loss of ~30%, for 14D there was a weight loss of ~25%, and for 30D there was a weight loss of ~26%. Again, there appear to be significant differences between 2D and 14D/30D, but the difference between 14D and 30D is probably below experimental error. We note that although differences are observed, they provide an incomplete picture of the thermal behavior of the sample as it ages. Consideration of the derivative of weight loss with respect to temperature provides a better picture of the thermal decomposition behavior of the samples and of the effect of aging on such behavior. As shown in the **Figure 5**, the derivative weight loss clearly shows that thermal decomposition occurs in two broad steps, with the higher temperature step showing a series of smaller events. In analyzing the data in this figure we focus on three regions of interest: 100 to 250 °C, 250 to 300 °C, and 300 to 400 °C. No significant differences were observed in the first temperature range, with all samples showing a derivative weight loss peak at about 200 °C. This first peak could be attributed to the dissociation of one oleate ligand from the metal-oleate complex by CO_2 elimination and formation of metastable nuclei[1, 100]. Small differences were observed for all samples in the second temperature range, observing derivative weight

loss peaks at 262 and 290 °C for the iron-cobalt oleate aged for 2 days; 260 and 280 °C for the iron-cobalt oleate aged for 14 days; and 290 °C for the iron-cobalt oleate aged for 30 days. These derivative weight loss peaks could be attributed to the dissociation of free or weakly bound oleate molecules[1].   Significant differences were observed in the third temperature range, with several derivative weight loss peaks at 298, 335, and 376 °C for the iron-cobalt oleate aged for 2 days; 299 and 350 °C for iron-cobalt oleate aged for 14 days; and 305, 325, 340, 350, and 375 °C for the iron-cobalt oleate aged for 30 days. These peaks could be attributed to the dissociation of the remaining oleate ligands and formation of nanoparticles[1, 100]. Note that the synthesis of cobalt ferrite nanoparticles is carried out at 320 °C and only sample 30D exhibited well-defined derivative weight loss peak at 305 and 325 °C.

. **Differential Scanning Calorimeter:** Differential scanning calorimetry was also used to study the thermal decomposition behavior of the aged iron-cobalt oleate. **Figure 6** shows these measurements. For the iron-cobalt oleate aged for 2 days, small endothermic peaks at 220 and 280 °C, and a broader peak at 380 °C were observed. In the case of the iron-cobalt oleate aged for 14 days, small endothermic peaks were observed at 180 and 220 °C. Additionally, two broader peaks were observed at 305 and 380 °C. After aging for 30 days, the iron-cobalt oleate presented a small endothermic peak at 200 °C, a sharp peak at 310 °C, and a broader peak at 380 °C. Park and coworkers [100] reported endothermic peaks at 230 and 320 °C for an iron-oleate complex. These temperatures were associated with the nucleation and growth stages, which lead to the formation of monodisperse nanoparticles. Bao and coworkers[1]

observed an additional broader peak at 380 °C, which they claimed to correspond to the maximum temperature required to achieve complete decomposition or restructuring of the iron-oleate complex.
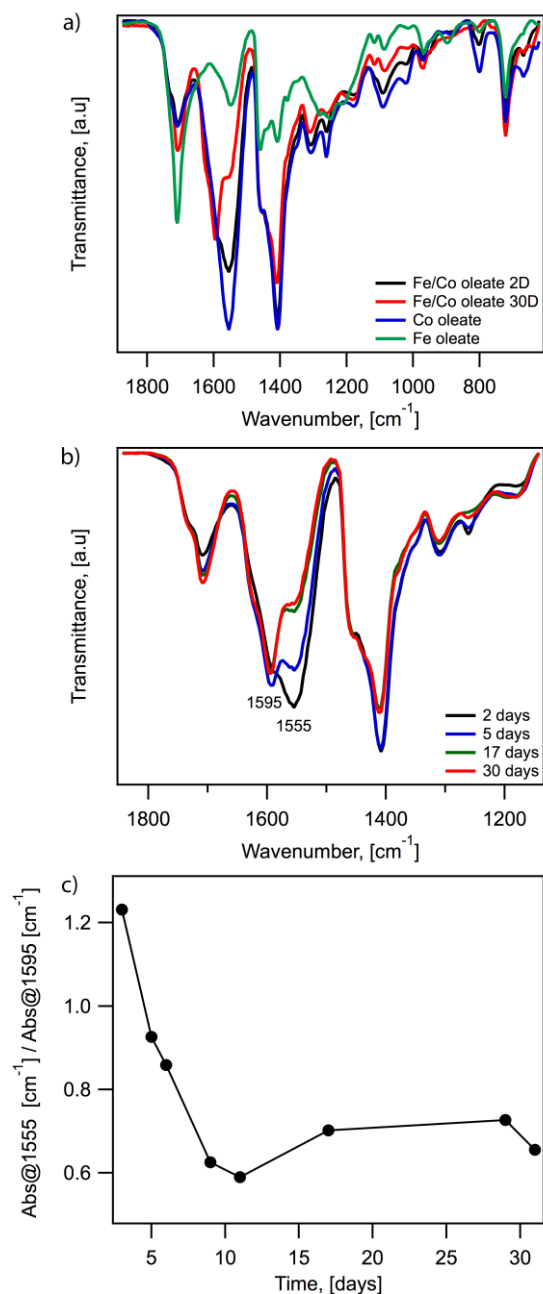
Figure 4.- a) FTIR spectra for the iron-cobalt oleate aged 2 and 30 days, and for an iron and a cobalt oleate. b) FTIR spectra for an iron-cobalt oleate aged over a period of 30 days. c) Ratio of the absorbances at 1555 cm^{-1} and 1595 cm^{-1} for an iron-cobalt oleate aged over a period of 30 days.
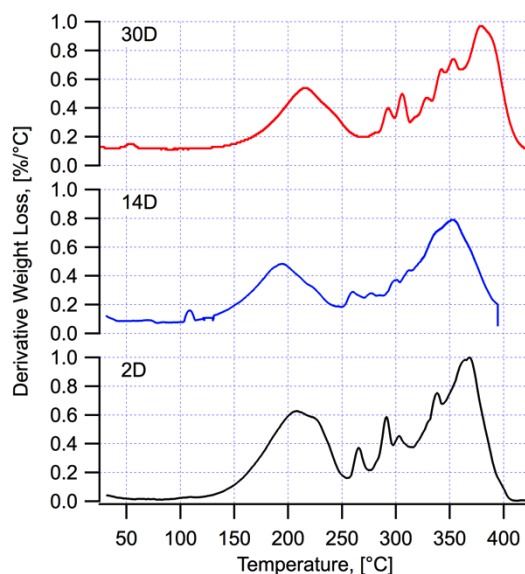
Figure 5.- Derivative weight loss from TGA measurements for iron-cobalt oleate after aging times of 2 days, 14 days, and 30 days. Measurements were performed at a heating rate of 3.5 °C/min

We remark on the asymmetric shape and the breadth of the peaks observed in the **Figure 6**, particularly the peak occurring between 200 and 300°C. A sharp change in heat flow in the DSC thermogram would correspond to an event that requires a significant amount of heat while the temperature remains constant, such as a phase transition or a dissociation reaction (e.g., an oleic acid ligand leaving the oleate group). The presence of a "tail" after the event could be evidence of heterogeneity in the characteristic temperature for such events. If all the molecules that undergo the transition do so at a well-defined temperature then one would expect a sharp peak. If there were a distribution of transition temperatures one would expect a broader peak. An asymmetric peak as we observe would indicate a fraction of molecules with similar transition temperature and a fraction of molecules with a distribution of higher transition temperatures. In the context of our measurements with oleates, it is interesting to note

that for the oleate aged for 2 days the first "peak" begins at a low temperature (~280°C) and has a very broad high temperature tail. As the aging time increases the low temperature side of the peak becomes sharper and the high temperature tail appears to become less pronounced, and at 30D a rather sharp peak is observed. This could be interpreted to indicate that as the oleate ages the coordination of the oleic acid to the iron and cobalt ions becomes more uniform throughout the sample. Regarding the peak at higher temperature (~380C), we do not observe as marked a change as the sample ages. This peak remains rather broad, which could be due to sequential removal of two remaining oleic acid ligands.
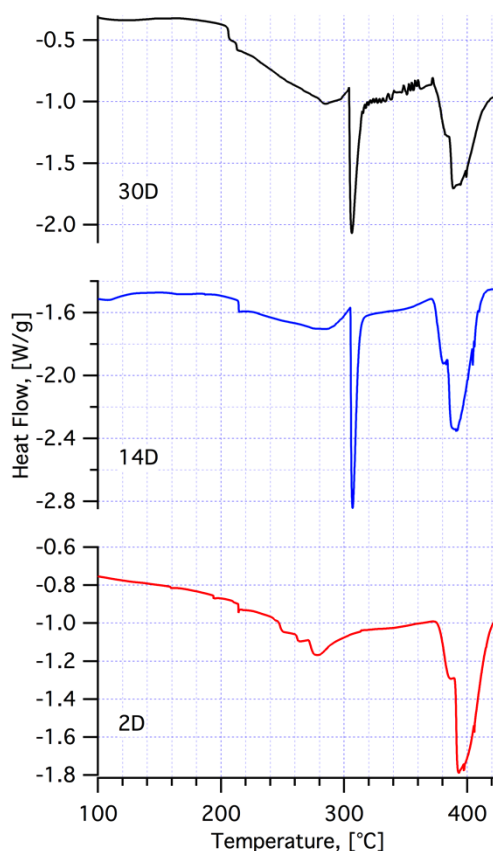
Figure 6.- DSC measurements for iron-cobalt oleate after aging times of 2 days, 14 days, and 30 days. Measurements were performed at heating rate of 20 °C/min.

Iron-cobalt nanoparticles

Nanoparticle size: The hydrodynamic diameter was measured for the synthesized cobalt ferrite nanoparticles in hexane. For these measurements, average hydrodynamic diameters D_h and standard deviations σ were determined from

$$D_h = \frac{\sum DG_d}{\sum G_d} \ , \ \sigma = \left[\frac{\sum \left(G_d \left(D_h - D \right)^2 \right)}{\sum G_d} \right]^{0.5} \ , \tag{4.1}$$

where D is the particle size obtained from the multimodal size distribution (MSD) function of the instrument and G_d is the relative intensity .The hydrodynamic diameters were determined to be 20 ± 2 nm for sample 2D, 19 ± 2 nm for sample 14D, and 17 ± 1 nm for sample 30D. **Table 2** summarizes these results, along with diameters obtained by other techniques such as XRD, magnetic characterization and TEM.

The physical size and size distribution of the synthesized magnetic nanoparticles was determined by transmission electron microscopy (TEM). The ImageJ program was used to measure the diameters of about one thousand nanoparticles (histogram shown in **Appendix A2 and A3**). **Figure 7** presents representative images of the synthesized cobalt ferrite nanoparticles, showing formation of separate nanoparticles with a narrow size distribution and a size of 12 ± 2 nm for sample 2D, 14 ± 2 nm for sample 14D, and 14 ± 5 nm for sample 30D.

The equilibrium magnetization response of cobalt ferrite nanoparticles suspended in hexane was recorded at 300 K. Non-linear regression was used to determine the magnetic core size D_m of the synthesized nanoparticles by curve fitting with the Langevin function weighted by the lognormal distribution [103, 104]. The magnetic core diameter was 10 ± 1 nm for sample 2D, 12 ± 1 nm for sample 14D, and 12 ± 1 nm for sample 30D. These diameters are in good agreement with the diameters determined from TEM (see **Table 2**).

Table 2.- Size distributions of the synthesized cobalt ferrite nanoparticles

Sample	$^a D_h$ (nm)	$^b D_p$ (nm)	$^c D_m$ (nm)	$^d D_c$ (nm)
2D	20 ± 2	12 ± 2	10 ± 1	5 ± 1
14D	19 ± 2	14 ± 2	12 ± 1	10 ± 1
30D	17 ± 1	14 ± 5	12 ± 1	12 ± 1

a Hydrodynamic size (Dh) measured using DLS. b Physical size (Dp) determined by TEM. c Magnetic core diameter (Dm) determined by the equilibrium magnetization of suspensions of nanoparticles in hexane at 10%w/w and 300 K. d Crystal size (Dc) determined from X-ray powder diffraction.
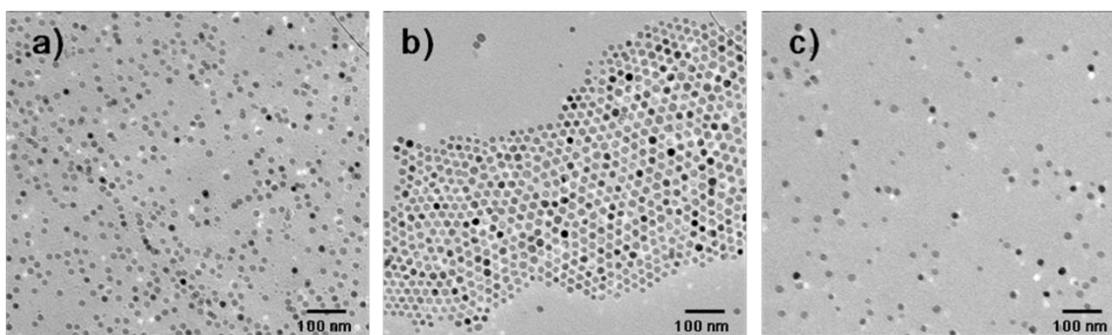
Figure 7.- TEM images of cobalt ferrite nanoparticles synthesized using iron-cobalt oleate aged at room temperature for a) 2 days (sample 2D), b) 14 days (sample 14D), and c) 30 days (sample 30D).

Nanoparticle structure and composition.

XRD: X-ray powder diffraction was used to verify the crystalline structure and determine the crystal size of the synthesized nanoparticles. **Figure 8** shows the diffraction patterns of dry powder samples analyzed using Jade 8.0 to obtain the crystal size D_c (**Table 2**) and interplanar spacing d_{hkl} (**Table 3**). Crystal sizes of 5 ± 1 nm were obtained for sample 2D, 10 ± 1 nm for sample 14D, and 12 ± 1 nm for sample 30D. Note that in the case of sample 2D, its crystal size is much smaller than the physical size determined from TEM and the magnetic core size determined from the equilibrium magnetization.

To verify the crystallinity of the synthesized nanoparticles, we calculated the lattice parameter *a* using the interplanar spacing d_{hkl} and Bragg's law [105],

$$a = d_{hkl} \sqrt{h^2 + k^2 + l^2} \ . \tag{4.2}$$

Table 3 reports the calculated lattice parameters of the different plane peaks, showing excellent agreement between the lattice parameters of sample 30D and the values reported for the crystalline structure of bulk cobalt ferrite [106]. In the case of sample 14D there was a slight difference between the lattice parameters and the reported bulk values. This difference was even greater for sample 2D, which indicates that aging of the iron-cobalt oleate influences the crystalline structure of the synthesized nanoparticles, longer aging promoting formation of the correct structure. These

observations are represented graphically in the XRD patterns in **Figure 8**, where it can also be observed that sample 2D exhibits peaks at positions and relative intensities that are different from the representative peaks of the cobalt ferrite standard. Diffraction peaks at scattering angles (2Θ) of 42.2° and 61.5°, could be due to scattering from the [200] and [220] planes of a cobalt oxide crystal lattice[107]. This observation indicates that sample 2D may consist of a mixture of cobalt ferrite nanoparticles and a cobalt oxide impurity.

Table 3.- Lattice parameter, a (Å), and inter-planar distance, d_{hkl} (Å), of nanoparticles and bulk cobalt ferrite.

Sample	d_{220}	d_{311}	d_{400}	d_{511}	d_{440}	a_{220}	a_{311}	a_{400}	a_{511}	a_{440}
2D	2.89	2.56	--	1.62	--	8.17	8.49	--	8.42	--
14D	2.95	2.52	2.09	1.61	1.48	8.34	8.36	8.36	8.37	8.37
30D	2.97	2.53	2.10	1.61	1.48	8.40	8.39	8.40	8.37	8.37
CoFe$_2$O$_4$ bulk [106]	2.97	2.53	2.08	1.61	1.48	8.40	8.39	8.32	8.37	8.37

Inductively coupled plasma optical emission spectroscopy (ICP-OES) was used to assess the incorporation of cobalt and iron into the synthesized nanoparticles. From these measurements we determined that the experimental Fe:Co ratio in all samples was higher than the stoichiometric ratio of 2.0. This implies that cobalt was not totally incorporated into the ferrite structure of the synthesized nanoparticles and hence cobalt substituted ferrites $Co_xFe_{3-x}O_4$ were produced.

The calculated *x* values of the synthesized nanoparticles were 0.92 for sample 2D, 0.78 for sample 14D, and 0.90 for sample 30D. Note that in the case of sample 2D, Xray diffraction measurements indicates the presence of a cobalt oxide phase, thus the actual ferrite particles may have a lower *x* value. However it is impossible for us to separate these two phases in order to ascertain this possibility.
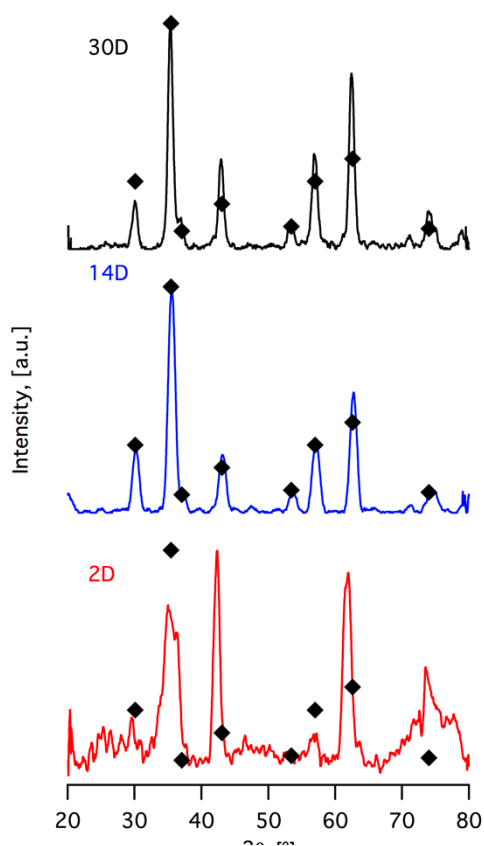
Figure 8.- X-ray powder diffraction patterns spectrum: illustrates the diffraction pattern of nanoparticles synthesized with oleate aged for 2 days, 14 days and 30 days. In all spectra, diamonds represent the diffraction peak positions for a cobalt ferrite standard.

Mössbauer analysis: **Figure 9** shows Mössbauer spectra of powder samples of cobalt ferrite nanoparticles recorded at room temperature. These measurements revealed spectra with sextet peaks for all the samples. While the spectra for sample 14D (**Figure 9.b**) and 30D (**Figure 9.c**) were well resolved with clearly discernible overlapping peaks associated with octahedral and tetrahedral Fe site occupation, the spectra for sample 2D (**Figure 9.a**) revealed higher peak asymmetry between the right-hand-side and left-hand-side portions of the spectrum, which was accompanied with a broad central portion. This can be attributed to the poor resolution of Fe sites within the material. In addition to poor crystallinity (which would lead to large distribution of Fe sites), it is possible that loose atomic arrangements on the surfaces could result in poor resolution and the observed peak asymmetry. The central portion of the spectrum of sample 2D exhibited paramagnetic doublet peaks due to single domain particle size phenomenon associated with superparamagnetism at room temperature. It is evident that the crystallinity of the synthesized nanoparticles is affected by the aging time of the iron-cobalt oleate precursor. It is expected that magnetic properties would be similarly influenced.

These measurements were analyzed using WMOSS software and the hyperfine distribution model according to Rancourt and Ping [101]. The fitting for sample 2D revealed that this sample was populated by octahedral and tetrahedral Fe sites that accounted for 21.6% and 32.7%, respectively, with the superparamagetic component accounting for 45.7%. Sample 14D was fitted with the octahedral Fe site corresponding to an internal magnetic field of 489.7 kOe while that of the tetrahedral site was 457.2

kOe. Their respective relative abundances were 48.9% and 49.3%, while the insignificant component associated with superparamagnetism accounted for 1.8% of the sample. The near equi-abundance of the magnetically ordered sites in comparison to sample 2D is indicative of the association of cationic distribution as a function of aging time of the precursor materials. This line of reasoning is backed by the fact that sample 30D was fitted with octahedral and tetrahedral Fe sites. The internal magnetic field of this sample was 585.7 kOe and 471 kOe, respectively; with relative abundances of 24.7% and 67.1%. Though the superparamagnetic component accounted for about 8% of the total spectrum, it appears that the tetrahedral site occupation increased with increasing aging time, while this was not the case for the octahedral site.

Magnetic properties: The equilibrium magnetization, coercivity, and reduced remanence of cobalt ferrite nanoparticles were determined at 2, 300, and 400 K by immobilizing the synthesized nanoparticles in a solid matrix of poly(styrene-divinylbencene) at 1 % w/w [102]. Sample magnetization was normalized by the inorganic core mass, as determined by thermo-gravimetric analysis (TGA) (**Appendix A4**). **Table 4** summarizes the results of magnetic characterization. Samples at 2 K displayed ferromagnetic behavior, as illustrated in **Figure 10.a)**, with a saturation magnetization of 19 Am^2kg^{-1} and coercivity of $6.6 \times 10^5 \, Am^{-1}$ for sample 2D, saturation magnetization of 27 Am^2kg^{-1} and coercivity of $6.2 \times 10^5 \, Am^{-1}$ for sample 14D, and saturation magnetization of 63 Am^2kg^{-1} and coercivity of $16.3 \times 10^5 \, Am^{-1}$ for sample 30D. At 300 K all samples exhibited ferromagnetic behavior, but their saturation magnetization and coercivity both decreased, as shown in **Figure 10.b)**. We observed

a saturation magnetization of 9.8 Am^2kg^{-1} and coercivity of 3.4×10^3 Am^{-1} for sample 2D,

saturation magnetization of 7.0 Am^2kg^{-1} and coercivity of 8.6×10^3 Am^{-1} for sample 14D,

and saturation magnetization of 50 Am^2kg^{-1} and coercivity of 4.4×10^4 Am^{-1} for sample

30D. No coercivity was observed for samples at 400 K, as illustrated in **Figure 10.c)**,

and the saturation magnetization further decreased, displaying values of 8 Am^2kg^{-1} for

sample 2D, 6.0 Am^2kg^{-1} for sample 14D, and 47 Am^2kg^{-1} for sample 30D. Note that at

the selected temperatures (2, 300, and 400K), the saturation magnetization of sample

30D was always higher than the values recorded for samples 2D and 14D (**Table 4**).

This can be related to a decrease of surface disorder in sample 30D, as this sample

displayed an excellent agreement between crystalline lattice parameters and the values

reported for the crystalline structure of bulk cobalt ferrite. Also, this sample showed

good agreement between its physical size D_p, magnetic core diameter D_m, and crystal

size D_c (**Table 2**).

The reduced remanence, or squareness (SQ = Mr/Ms), of the synthesized

nanoparticles was determined at 2 and 300 K (Table 3). At 2 K, we calculated a SQ of

0.35 for sample 2D, 0.25 for sample 14D, and 0.70 for sample 30D. In the case of

samples at 300 K, we calculated a SQ of 0.03 for sample 2D, 0.13 for sample 14D, and

0.28 for sample 30D. A theoretical SQ value of 0.5 is attributed to single domain

magnetic nanoparticles with uniaxial anisotropy, while SQ values of 0.83 indicate the

presence of cubic magnetocrystalline anisotropy, as is the case of bulk cobalt ferrite [6,

108, 109].   In our case, the synthesized nanoparticles exhibited uniaxial

magnetocrystalline anisotropy, as all samples displayed a *SQ* value less than 0.8; however an increase in *SQ* was observed with aging time of the oleate precursor.

The blocking temperature T_B of the synthesized magnetic nanoparticles was estimated from zero-field-cooled (ZFC) and field-cooled (FC) measurements obtained at an applied field of 1 mT in the temperature range of 2 to 400 K. **Figure 11** shows these measurements.

For sample 2D we observed two peaks in the ZFC curve, one at 48 K and another at 308 K (**Figure 11.a**). It is possible that the low temperature peak corresponds to a cobalt oxide impurity present in the sample, since the superparamagnetic blocking temperature of Co-CoO has been reported below 50 K [110]. In the case of sample 14D, we do not observe the presence of the low temperature peak, but the ZFC curve looked broader with a maximum at 354 K (**Figure 11.b**) and a shoulder at ~200 K. In sample 30D, no peak was detected in the ZFC curve indicating that it should be above 400 K **(Figure 11.c)).**

The temperature corresponding to the peak of the ZFC curves is often associated with the blocking temperature T_B of the nanoparticles, from which one can estimate the magnetic anisotropy constant K using
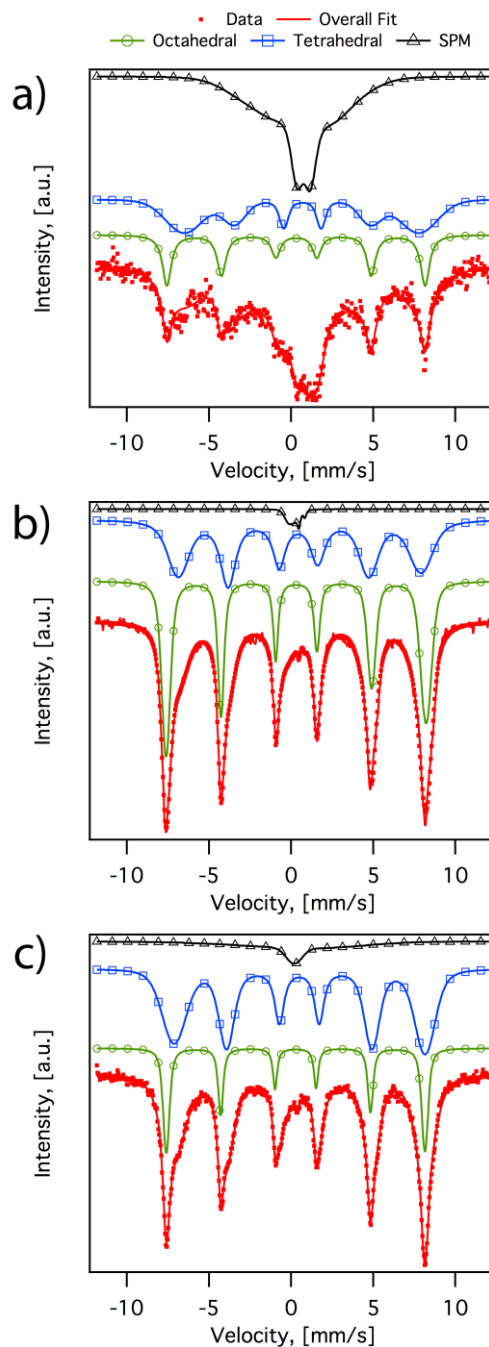
Figure 9.- Mössbauer spectra of cobalt ferrite nanoparticles. Spectrum a) illustrates nanoparticles synthesized with oleate aged for 2 days, b) shows nanoparticles synthesized with oleate aged for 14 days, and c) illustrates nanoparticles synthesized with oleate aged for 30 days. In all spectra circles represent the superparamagnetic component, diamonds indicate the tetrahedral sites, triangles indicate the octahedral Fe site, dots illustrate the collected data, and the black solid line indicates the overall fit

.

$$K = \frac{T_B k \ln\left(\dfrac{\tau_m}{\tau_0}\right)}{V_m}, \qquad\qquad (4.2)$$

Where V_m is the volume of the magnetic nanoparticle core and τ_m is the experimental measurement time, usually taken as 100 s. Using the magnetic core size D_m of the synthesized nanoparticles, obtained at 300 K by curve fitting with the Langevin function weighted by the lognormal distribution (**Table 2**), and the blocking temperature T_B obtained from the ZFC curve (308 K for sample 2D and 354 K for sample 14 D), we estimated a magnetic anisotropy constant K of 176.2 kJ.m^{-3} for sample 2D and 134.2 kJ.m^{-3} for sample 14D, both of which are smaller than the magneto-crystalline anisotropy constant of bulk cobalt ferrite (200 kJ.m^{-3} [111]). Note that sample 2D exhibited a lower blocking temperature and higher magnetic anisotropy constant as compared with sample 14D. This is because the magnetic core size and crystal size determined for sample 2D were both smaller than the sizes determined for sample 14D (**Table 2**). In the case of sample 30D, as no peak was observed in the ZFC curve, we estimate its blocking temperature assuming that the magneto-crystalline anisotropy constant K of this sample is the same as that of bulk cobalt ferrite, (200 kJ.m^{-3}). Using a magnetic core size of 12 nm (**Table 2**), a blocking temperature T_B of 569 K was estimated from **Eq. (4.2)**. This is outside the temperature range accessible with our instrument.

To study the magnetic relaxation mechanism and time of the nanoparticles we measured their AC susceptibility as a function of applied field frequency, as illustrated in

Figure 12. Cobalt ferrite nanoparticles synthesized using oleate aged for 2, 14, and 30 days were suspended at 10 % w/w in mineral oil at 273 K (viscosity of 0.816 Pa.s). The AC susceptibility measurements of the suspended nanoparticles were interpreted using the Debye model. We observed peaks in χ" at 126 Hz for sample 2D (**Figure 12.a**), 100 Hz for sample 14D (**Figure 12.b**), and 63 Hz for sample 30D (**Figure 12.c**). Applying the condition $\Omega\tau = 1$ at the maximum of the χ" curve we determined experimental relaxation times τ_{exp} of 1.3×10^{-3} s for sample 2D, 1.6×10^{-3} s for sample 14D, and 2.5×10^{-3} s for sample 30D (**Table 5**). For comparison purposes, we calculated the Brownian relaxation time of these nanoparticles, τ_B, by using Eq. (2) and the hydrodynamic size of the nanoparticles obtained from DLS measurements (**Table 2**), resulting in a Brownian relaxation time of 2.7×10^{-3} s for sample 2D, 2.3×10^{-3} s for sample 14D, and 1.7×10^{-3} s for sample 30D, all of which are of the same order of magnitude as the experimental Brownian relaxation times obtained from the AC susceptibility measurements (**Table 5**).
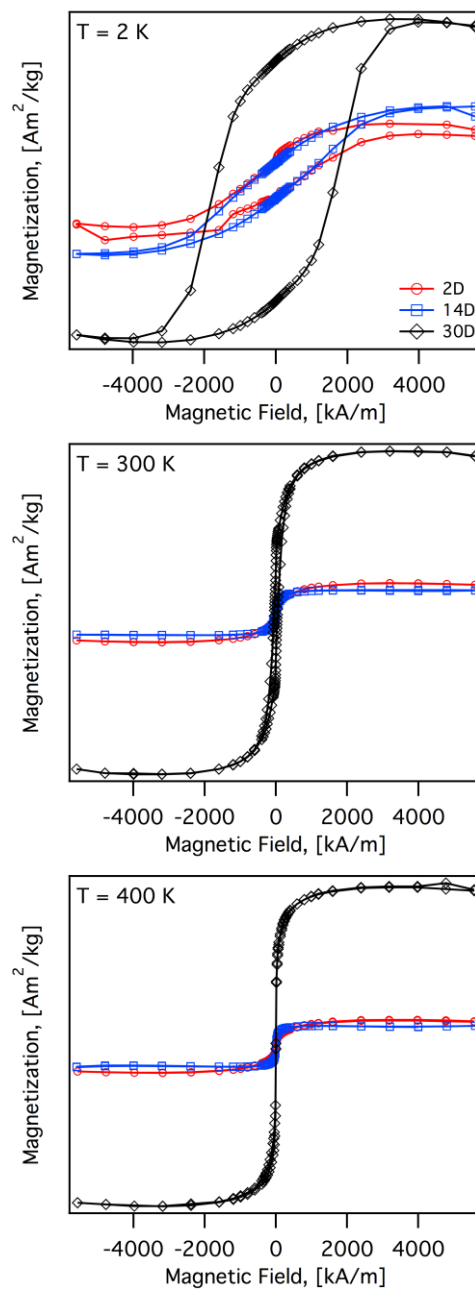
**Figure 10**.- Magnetization of CoFe$_2$O$_4$ nanoparticles immobilized in poly(styrene-divinyl-benzene) at 1% w/w. Sample magnetization was normalized by the magnetic core mass, as determined by TGA. Circles (○) represent nanoparticles synthesized using oleate aged for 2 days. Triangles (Δ) represent nanoparticles synthesized using oleate aged for 14 days. Squares (□) illustrate nanoparticles synthesized using oleate aged for 30 days.

Table 4.- Coercivity *Hc*, saturation magnetization *Ms*, and reduced remanence *Mr/Ms* of cobalt ferrite nanoparticles immobilized in poly(styrene-divinyl-benzene) at 1% w/w at different temperatures

Sample	2K				300K				400K
	Hc (Am^{-1})	Mr (Am^{2}kg^{-1})	Ms (Am^{2}kg^{-1})	$\frac{Mr}{Ms}$	Hc (Am^{-1})	Mr (Am^{2}kg^{-1})	Ms (Am^{2}kg^{-1})	$\frac{Mr}{Ms}$	Ms (Am^{2}kg^{-1})
2D	6.6×10^5	6.6	19	0.35	3.4×10^3	0.3	10	0.03	8
14D	6.2×10^5	6.6	27	0.25	8.6×10^3	0.9	7	0.13	6
30D	16.3×10^5	45	63	0.70	4.4×10^4	14	50	0.28	47

.

Table 5.- Relaxation times of cobalt ferrite nanoparticles suspended in mineral oil at 10 %w/w and 273 K.

Sample	τ_{exp} (s)	τ_B (s)	K (kJm^{-3})	τ_N (s)	χ''_{max}/χ_0
2D	1.3×10^{-3}	2.7×10^{-3}	176.2	1.9×10^2	0.35
14D	1.6×10^{-3}	2.3×10^{-3}	134.2	9.3×10^3	0.43
30D	2.5×10^{-3}	1.7×10^{-3}	---	7.0×10^{11}	0.44

*Here, τ_{exp} is the experimental relaxation time determined from the peak of the χ'' curve; τ_B is the Brownian relaxation time calculated from the hydrodynamic diameter of the synthesized nanoparticles and Eq.(2); *K* is the magnetic anisotropy constant calculated from the ZFC/FC curves; τ_N is the Néel relaxation time calculated from *K* (in the case of sample 30D, we assumed a *K* value of 200 kJ.m-3, which corresponds to bulk cobalt ferrite [111]); and χ''_{max}/χ_0 is the ratio between the components of the AC susceptibility at the peak of χ'' curve.
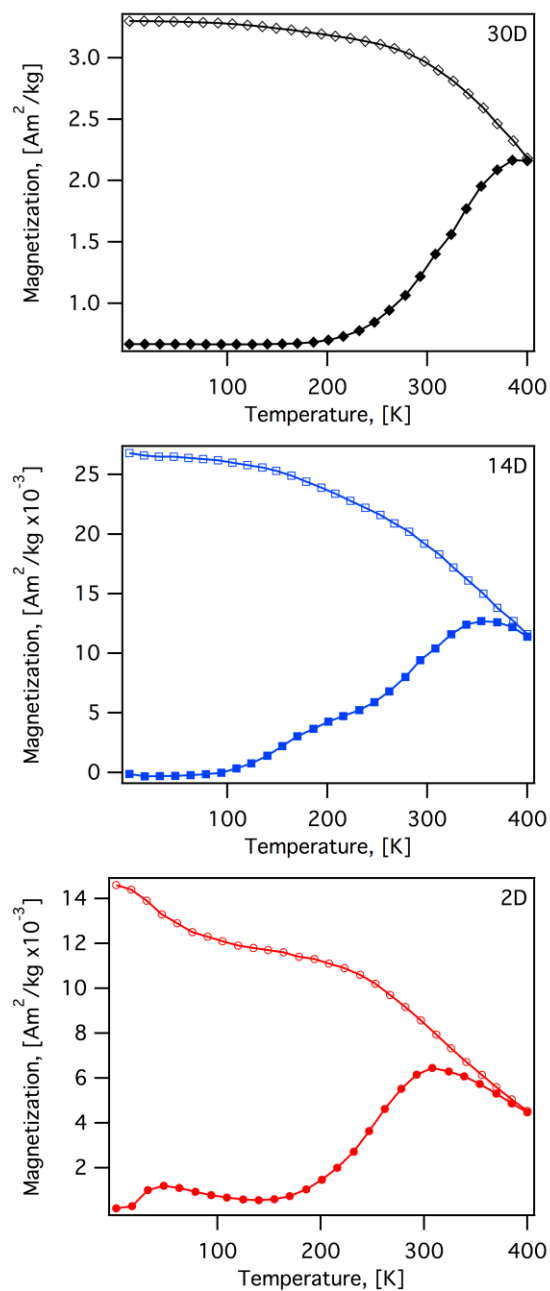
Figure 11.- Temperature dependent magnetization of cobalt ferrite nanoparticles under zero field cooled (ZFC) and field cooled (FC) conditions at 1 mT.

Samples were immobilized in polystyrene-divinyl-benzene (pSDVB) at 1%w/w and heated up to 400 K in zero field before measurements. Cobalt ferrite nanoparticles

synthesized using oleate aged for 2 days (sample 2D) exhibited a blocking temperature at 308 K from the ZFC curve. Nanoparticles synthesized using oleate aged for 14 days (sample 14D) exhibited a blocking temperature at 354 K from the ZFC curve. No blocking temperature could be determined for nanoparticles synthesized using oleate aged for 30 days (sample 30D) in the measured temperature range.

For comparison purposes, the Néel relaxation time of the magnetic nanoparticles was calculated using the value of the magnetic anisotropy constant K estimated from the blocking temperature T_B and **Eq. (4.2)**, resulting in a Néel relaxation time of 1.9×10^2 s for sample 2D and 9.3×10^3 s for sample 14D (**Table 5**). In the case of sample 30 D, we estimated a Néel relaxation time of 7.0×10^{11} s assuming that the magneto-crystalline anisotropy constant K of this sample is the same as the bulk cobalt ferrite (200 kJ.m^{-3}).

It is commonly assumed that magnetic relaxation occurs through the faster of the two mechanisms. Particles for which $\tau_B \ll \tau_N$ relax through the Brownian mechanism and are said to have their magnetic dipoles "thermally blocked". Comparing the relaxation times (Table 4), we can infer a Brownian relaxation mechanism for the synthesized cobalt ferrite nanoparticles, as the Brownian relaxation times (experimental and calculated) are smaller than the calculated Néel relaxation time.
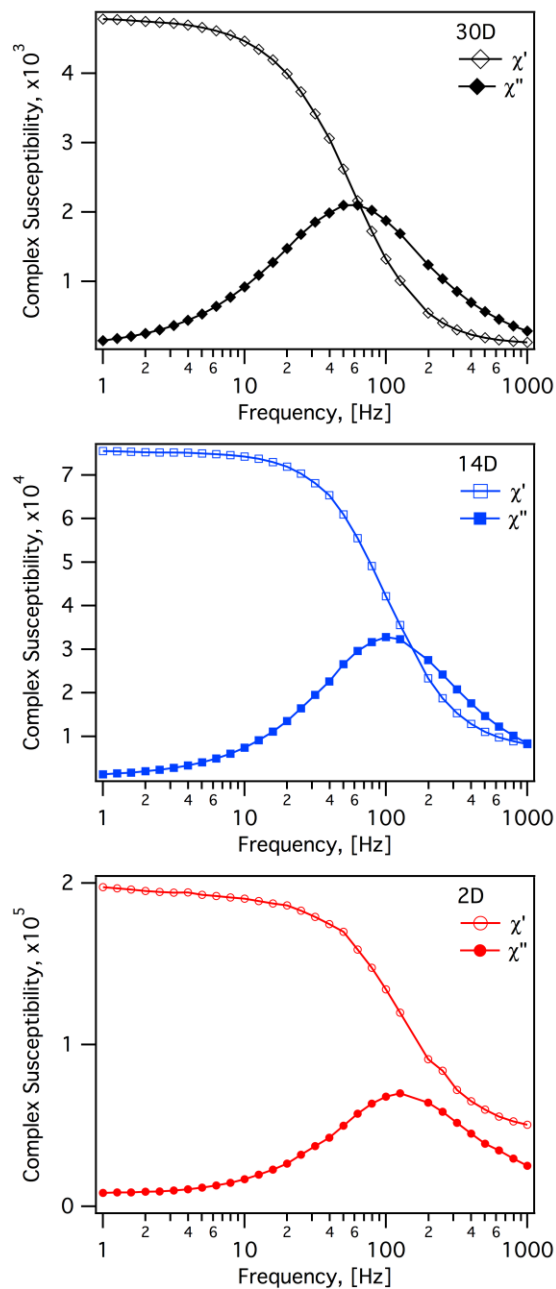
Figure 12.- AC susceptibility measurements of cobalt ferrite nanoparticles suspended in mineral oil at 10 %w/w and 273 K. a) 2D, b) 14D, and c) 30D. Open circles ($\circ$) represent the in-phase component χ' and fill circles ($\bullet$) represent the out-of-phase component χ'' of the complex susceptibility

According to theory, nanoparticles with a single relaxation mechanism ($\chi_\infty = 0$) exhibit

a ratio $\chi''_{\max}/\chi_0$ of 0.5, visually confirmed by crossing of the curves of the in-phase χ' and

out-of-phase χ'' components of the complex susceptibility at the peak of χ'' [112, 113]. **Figure 12** shows that aging of the iron-cobalt oleate precursor improved the AC susceptibility properties of the synthesized cobalt ferrite nanoparticles, as sample 14D and sample 30D displayed crossing of the components of the complex susceptibility. **Table 5** reports the ratio χ''_{max} / χ_0, which was 0.35 for sample 2D, 0.43 for sample 14D, and 0.44 for sample 30D, indicating that iron-cobalt aging resulted in nanoparticles with increasingly predominant Brownian relaxation.

4.4 Conclusions

Together, the FTIR, TGA, and DSC results presented above provide a picture of the chemical changes the iron-cobalt oleate undergoes during aging. FTIR spectra indicate that cobalt oleate contains primarily oleates in a bidentate conjugation with cobalt ions, whereas iron oleate contains a mixture of bidentate and bridging coordination. In the iron and cobalt oleates there does not appear to be a significant change in this coordination with aging. On the other hand, FTIR spectra for the iron-cobalt oleate indicated there was a change in the prevalence of the two coordination modes as the sample aged. Initially the peak associated with bidentate conjugation appeared more pronounced, but with aging time this peak decreased in magnitude relative to the peak corresponding to bridging coordination. We believe that initially most of the cobalt ions in the iron-cobalt oleate are in a bidentate conjugation with the oleate, whereas the iron ions are in both bidentate and bridge coordination. Furthermore, we believe that as the sample ages the coordination with the cobalt ions changes to bridging coordination,

resulting in oleate molecules interacting with iron-iron, iron-cobalt, and cobalt-cobalt ion pairs. This hypothesis is consistent with the DSC results wherein we observed a broad endotherm between 200 and 300°C for the sample at 2 days, with significant narrowing of the endotherm (and shifting to higher temperature) as the sample ages. As noted, a broad endotherm could be the result of a wide distribution of decomposition temperatures in the sample, which would be consistent with a sample with heterogeneity in term of oleate-metal ion coordination modes. As the oleate-metal ion coordination modes become more uniform throughout the sample the distribution of decomposition temperatures would narrow, resulting in a narrow endotherm in the DSC measurement.

Synthesis of monodisperse cobalt ferrite nanoparticles with well-defined Brownian relaxation is desirable for magnetic sensor applications and for nanoscale viscosity measurements. The thermal decomposition of an iron-cobalt oleate precursor appears as a good alternative to obtain cobalt ferrite nanoparticles with narrow size distribution. We studied the influence of aging of the oleate precursor to obtain cobalt ferrite nanoparticles with a narrow size distribution and that respond to changes in the magnetic field solely by the Brownian relaxation mechanism. It was observed that aging for up to 30 days resulted in changes in the coordination mode between the oleate molecules and the iron/cobalt ions, which in turn influenced the thermal behavior of the iron-cobalt oleate precursor and resulted in the formation of the correct crystal ferrite structure. It was also determined that cobalt ferrite nanoparticles synthesized using the iron-cobalt oleate aged for only 2 days showed poor agreement with the expected ferrite structure, possibly due to the presence of a contaminant phase which may be a cobalt

oxide. Furthermore, the crystal size and magnetic core size of this sample were lower as compared with the sizes determined for cobalt ferrite nanoparticles synthesized using the iron-cobalt oleate aged for 14 and 30 days. These differences in size and crystallinity led to differences in the magnetic properties of the synthesized nanoparticles, such as blocking temperature and magnetocrystalline anisotropy constant. It was determined that although all samples exhibited some degree of Brownian relaxation, aging of the iron-cobalt oleate precursor resulted in crossing of the in-phase χ' and out-of-phase χ'' components of the complex susceptibility, an attribute of a collection of nanoparticles with a single dominant magnetic relaxation mechanism. The resulting nanoparticles would be suitable for sensors based on the Brownian relaxation mechanism and in determining mechanical properties of complex fluids at the size scale of the nanoparticles.

5. Monitoring the local environment of magnetic nanoparticles in alternating magnetic fields

5.1 Monitoring iron oxide nanoparticle surface temperature in an alternating magnetic field using thermoresponsive fluorescent polymers.

In this study is reported the indirect measurement of the surface temperature of iron oxide nanoparticles in an alternating magnetic field (AMF) through the temperature induced change in fluorescence of a thermoresponsive/fluorescent polymer consisting of poly-(N-isopropylacrylamide) (pNIPAM) copolymerized with a fluorescent modified acrylamide (FMA) monomer with fluorescence intensity that increases as its surroundings change from hydrophilic to hydrophobic. When the particles are suspended in water and subjected to external heating, the fluorescence is observed to remain constant up to about 35°C, above which temperature it increases. When the particles dissipate heat internally in an AMF, the fluorescence intensity increases immediately upon application of the AMF, even though the temperature (as measured by an immersed fiber-optic probe) is below 35°C. The observed increase in fluorescence intensity indicates a change in the microenvironment of the FMA due to the transition of the pNIPAM from hydrophilic to hydrophobic. This in turn suggests that the nanoparticle surface temperature is above 35°C and therefore higher than the temperature of the surrounding medium.

By comparing fluorescence change with temperature during external heating and heating with an AMF we are able to demonstrate that the nanoparticle surface rises above the bulk temperature in an AMF because the thermoresponsive polymer undergoes its transition, reported by the change in fluorescence, at a bulk temperature that is much below the transition temperature observed when using external heating.

Previous work

It has been demonstrated that under equivalent thermal doses MFH is more effective in killing cancer cells in vitro than hyperthermia using a hot water bath[114]. Creixell et al (2011) [115] reported that epidermal growth factor (EGF)-conjugated (IO) nanoparticles targeting the epidermal growth factor receptor result in 99% reduction in cell viability and clonogenic survival when exposed to an AMF, without a perceptible rise in medium temperature. It has been suggested that intracellular hyperthermia has greater benefits over extracellular hyperthermia, however, Rabin (2002) argued that there should not exist any advantage to intracellular hyperthermia since the rate of energy dissipation is less than the rate of heat removal by conduction, resulting in a negligible rise in the surface temperature of the nanoparticle[116]. On the other hand, Huang et al (2010) demonstrated experimentally, using fluorophores as a nanometre-scale thermometer, that the surface temperature of iron oxide nanoparticles may heat significantly above that of their surroundings[117]. Finally, Polo-Corrales et al (2012) report indirect measurements of the surface temperature of iron oxide nanoparticles in

an alternating magnetic field (AMF) through the temperature induced change in fluorescence of a thermoresponsive/fluorescent polymer[118].

Magnetically triggered release of a controlled dose is expect to be more beneficial than passive diffusion or releases triggered by changes in the environment [119, 120] [121-124]. Amstad (2011) et al provide indirect evidence of local heating by iron oxide nanoparticles embedded in lipid membranes because the application of an AMF changed the membrane permeability without a significant rise in medium temperature[125].

5.1.1 Experimental section

Materials

N-isoprylacrylamide 97% was obtained from Sigma Aldrich and recrystallized with n-hexane twice. Chloride (III) hexahydrate (97% ACS reagent) was obtained from Across Organics. Chloride (II) tetrahydrate (99% ACS reagent), 2-(methylamino)-ethanol (98%) and 2, 2- azobisisobutyronitrile (AIBN 98%) were obtained from Sigma-Aldrich and used without further purification. 3-methacryloxypropyltrimethoxysilane (MPS) and 4-(N,N-Dimethylaminosulfonyl)-7-fluoro-2,1,3-benzoxadiazole (DBD-F) were obtained from Tokyo Chemical Industry. N, N' –Methylene-bisacrylamide (MBA 99%) was obtained from Aldrich and used without further purification.

Synthesis procedure

Iron oxide (IO) nanoparticles were prepared by co-precipitation of $FeCl_3*6H_2O$ and $FeCl_2*4H_2O$ through addition of ammonium hydroxide (0.2 M) while maintaining a temperature of 80°C. The magnetite nanoparticles were precipitated by centrifugation, peptized with tetramethylammonium hydroxide (1 M), and suspended in ethanol to form a stable solution. Afterwards, MPS, water, ammonium hydroxide and excess ethanol were added and the solution maintained in mechanical agitation at room temperature for 72 hours.

A fluorescent modified acrylamide monomer (FMA) was synthetized using DBD-F following the procedure reported by Uchiyama [75]. The fluorescent modified acrylamide monomer with a benzofurazan group was obtained by the reaction of DBD-F and methylethanolamide at room temperature for 30 minutes, then acryloyl chloride was added and the reaction took place at 60 °C for 12 hours.

Iron oxide nanoparticles functionalized with MPS were coated with a layer of thermoresponsive/fluorescent polymer by free radical polymerization of FMA in 10 ml acetone (5.8% w/v) and NIPAM in 20 ml acetone (7.5% w/v) in presence of 0.13 g of the crosslinker MBA in 20 ml of acetone and 0.08g of AIBN in 10 ml acetone as initiator. Following the technique reported by Herrera et al.,[74] all the solutions were added to a reactor and maintained at 60 °C for eight hours under continuous stirring at 200 rpm. After the reaction, the IO nanoparticles covered with p(NIPAM-co-FMA) were washed with diethyl ether: acetone using a ratio of 1:3 v/v.

5.1.2 Characterization

The infrared spectra of IO nanoparticles functionalized with MPS and p-(NIPAM-co-FMA) were obtained using an FT-IR (Bruker IF 66 V/S). The hydrodynamic diameter of IO functionalized with MPS and p-(NIPAM-co-FMA) coated IO nanoparticles were measured through Dynamic Light Scattering (DLS) using a Brookhaven Instruments BI-90Plus Particle Size Analyzer. The mass percentage of inorganic material in the nanoparticles was determined through thermogravimmetric analysis (TGA) using a TGA/DSC1 Thermogravimetric Analyzer from Mettler-Toledo.

The fluorescence intensity of the p-(NIPAM-co-FMA) coated IO nanoparticles was measured using an optical fiber probe (PRO-PROBE, BS-Ocean Optics) and the Spectra Suite program was used to collect data. A fiber-optic thermometer (LXT-m3300 BioMed Lab Kit-Thermometry Luxtron Corporation) was used to measure sample temperature. The alternating magnetic field was generated using an RDO Induction Power Supplies HFI 3 kW unit. A three-turn coil was used to generate field amplitudes of 38.4 kA/m at a frequency of 233 kHz. The coil was cooled using circulating water to approximately 20ºC.

5.1.3 Results

Analysis of MPS coated IO nanoparticle's FTIR spectra shows a band at 1110 cm^{-1} which is attributed to the Si-O-propyl bond to the magnetic core, a band at 1660 cm^{-1} indicating the presence of C=C on the nanoparticle, and a band at 1720 cm^{-1} which

is attributed to the vibration of the carbonyl group, indicating the presence of MPS in the nanoparticles. The p(NIPAM-co-FMA) coated IO nanoparticles show a band at 1550 cm^{-1} attributed[126] to amide II and the presence a band at 1730 cm^{-1} attributed to the vibration of the carbonyl group of the p(NIPAM-co-FMA) on the nanoparticle (see **Appendix A5)** TGA curves of the MPS coated magnetite nanoparticles and p(NIPAM-co-FMA) coated IO nanoparticles indicate that the mass percentage of inorganic material is 72% and 32%, respectively (see A**ppendix A6)**

The hydrodynamic diameter of the MPS coated IO nanoparticles in acetone was found to be 52 ±4 nm. The hydrodynamic size of the p-(NIPAM-co-FMA) coated IO in distilled water at 0.1% w/v was measured at temperatures ranging from 19 to 50 °C at temperature intervals of 2° C and with stabilization time of 2 minutes before each measurement. **Figure 13** shows the change in hydrodynamic diameter above and below the LCST, between 32°C and 36°C.
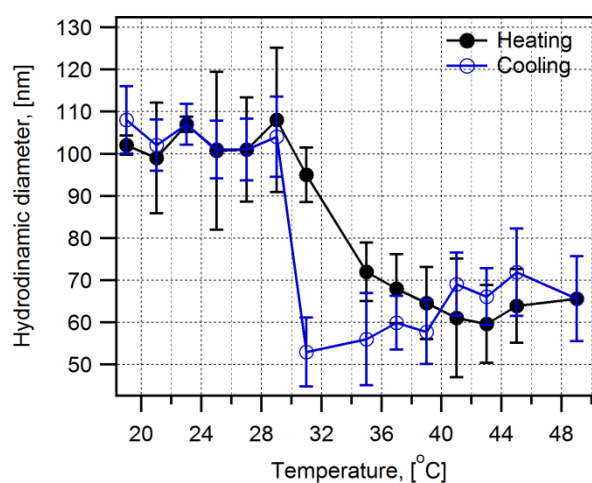

Figure 13.- Hydrodynamic diameter of p-(NIPAM-co-FMA) coated iron oxide nanoparticles in water as a function of temperature.

Figure 14 shows fluorescence intensity of the p-(NIPAM-co-FMA) IO nanoparticles as a function of temperature using external heating. The coated IO nanoparticles were concentrated to 1% w/v (magnetic core) in water and placed in a bath with external heating. Temperature increased in steps of 3°C, with temperature stabilization time of 5 minutes between each measurement. The FMA excitation wavelength was 460 nm and the FMA emission wavelength was 570 nm. The fluorescence intensity behavior shows a transition at about 35°C, near the LCST of pNIPAM (about 32°C) and in the range where hydrodynamic diameter changed with temperature, indicating an increase in the intensity of the FMA due to changes in the medium polarity when the pNIPAM is above the LCST.
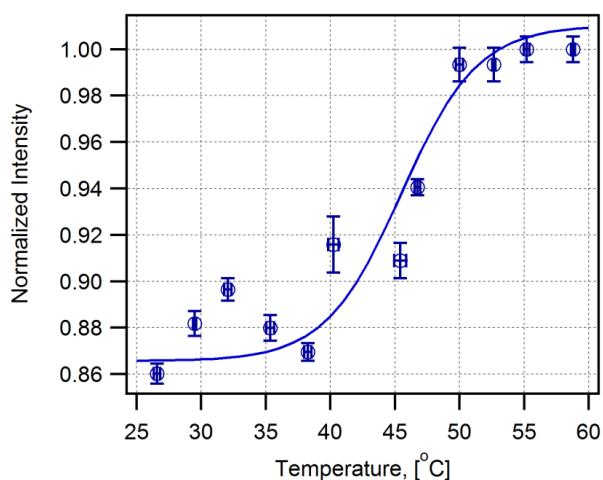
Figure 14.- Fluorescence intensity of p-(NIPAM-co-FMA) coated iron oxide nanoparticles at 1% w/v (magnetic core) in water under external heating

Figure 15 shows the fluorescence intensity (left axis) and temperature (right-axis) vs. time. A solution of p(NIPAM-co-FMA) coated IO nanoparticles at 1% w/v (magnetic core) in water were exposed to an alternating magnetic field of 38.4 (kA/m) and 233 kHz for 10 minutes (indicated by the dotted lines). During the first five minutes,

the AMF was off and no changes in temperature or fluorescence were observed. Next the AMF was turned on and a gradual rise in temperature to 45 °C was observed. However, it was observed that the fluorescence intensity increased immediately up AMF application, to a maximum value while the medium temperature was still in the range of 22 to 30 °C. This is shown in **Figure 15.b)** which shows the same data as **Figure 15.a)** but plotted as fluorescence intensity as a function of temperature in presence and in absence of the magnetic field. Afterwards, the fluorescence remained approximately constant in the temperature range of 30 to 34 °C (**Figure 15.b).** Next the fluorescence decreased in the temperature range of 34 to 45 °C. We suspect this decrease is due to aggregation resulting from the transition of pNIPAM to a hydrophobic state[127]. When the temperature reached 45 °C the AMF was turned off and the temperature and fluorescence decreased.
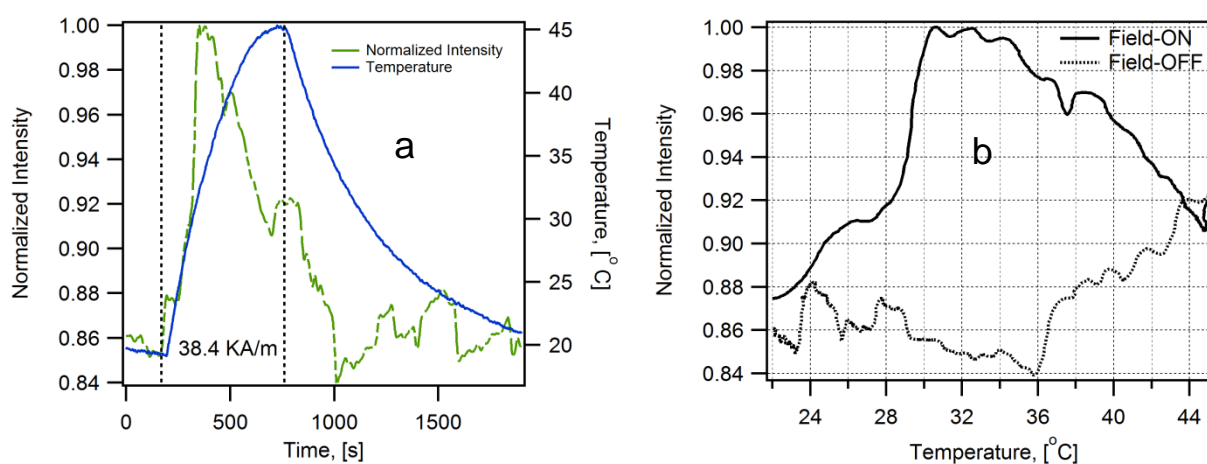

Figure 15.- (a) Temperature and fluorescence intensity of p(NIPAM-co-FMA) coated iron oxide nanoparticles (1% w/v (magnetic core) as a function of time with an AMF 38.4 (kA/m) and to a frequency 233 kHz. (b) Fluorescence intensity of p(NIPAM-co-FMA) coated IO nanoparticles.

5.1.4 Conclusions

In this study was observed indirect evidence of a rise in temperature in the vicinity of iron oxide nanoparticles exposed to an AMF, above that of the surrounding medium. To make these observations we prepared iron oxide nanoparticles coated with the fluorescent thermoresponsive polymer p(NIPAM-co-FMA). The fluorescence intensity change of the polymer reported the temperature in the immediate vicinity of the nanoparticles, whereas a fiber optic probe reported the temperature of the medium. When external heating was used the fluorescence intensity was observed to increase at a medium temperature above 35°C, whereas when an AMF was applied the fluorescence intensity was observed to increase immediately even while the medium temperature was close to 20°C. The observed change in fluorescence intensity indicated the p-(NIPAM-co-FMA) had crossed the LCST and hence that the temperature in its vicinity was significantly higher than that of the bulk solution.

5.2 Local Thermal Effects on the Surface of Magnetic Nanoparticles with different magnetic relaxation mechanisms.

We present experiments that explore the possibility of local thermal effects, conducted using magnetic nanoparticles which respond to alternating magnetic fields by either particle rotation (Brownian relaxation) or internal dipole rotation (Neel relaxation) and thermoresponsive fluorescent polymers acting as reporters of thermal events of the surface of the particles and in the bulk fluid. Our experiments demonstrate that there is indeed an immediate local thermal effect upon application of the alternating magnetic

field and that this effect is only active for one of the two nanoparticle magnetic relaxation mechanism.

5.2.1 Experimental section

Materials

N-isoprylacrylamide 97%(recrystallized twice with n-hexane), carboxymethyl-dextran sodium salt (CMDx), 1-ethyl-3-(3-dimethylaminopropyl) carbodiimide hydrochloride (EDC), N-hydroxysuccinimide (NHS) 98%, iron Chloride (II) tetrahydrate (99% ACS reagent), 2-(methylamino)-ethanol (98%), 2, 2- azobisisobutyronitrile (AIBN 98%), ammonium hydroxide (NH4OH) 29% v/v and tetramethylammonium hydroxide 25% w/v were obtained from Sigma-Aldrich. Cobalt chloride hexahydrate, 98% was purchased from Aldrich and used without further purification. Iron Chloride (III) hexahydrate (97% ACS reagent) was obtained from Across Organics. 3-methacryloxypropyltrimethoxysilane (MPS) and 4-(N, N-Dimethylaminosulfonyl)-7-fluoro-2, 1, 3-benzoxadiazole (DBD-F) were purchased from Tokyo Chemical Industry. N, N' –Methylene-bisacrylamide (MBA 99%) was obtained from Aldrich and used without further purification. 3-Aminopropyltriethoxysilane (APS) was obtained from TCI America without further purification.

Preparation of iron Oxide (IO) and Cobalt ferrite (ICO) nanoparticles

IO nanoparticles were synthesized by the co-precipitation method[115] using an aqueous iron solution at a 2.73 ratio of $Fe3^+$: Fe^{2+} in basic aqueous media with addition of ammonium hydroxide at 80 °C. The solution was stirred at 150 rpm at 80°C for 1 h, maintaining the pH between 8-8.5 by adding NH_4OH [0.2M] and deionized water. ICO nanoparticles were synthesized through co-precipitation[128] [10] of an aqueous $FeCl_3$ and $CoCl_2$ solution at a 2:1 ratio of Fe^{3+}: Co^{2+} by rapid addition to an excess of hydroxide ions under intensive heat. Afterwards, ICO nanoparticles were washed with deionized water and peptized using a hydrothermal treatment with boiling ferric nitrate at high temperature and agitation[129]. Both nanoparticle solutions were peptized with tetramethylamonium hydroxide [1M] to obtain negative surface charge on the nanoparticles.

Preparation of (Carboxymethyldextran) CMDX coated iron oxide and cobalt ferrite nanoparticles (IO-PS and ICO-PS)

The peptized nanoparticles were functionalized with APS in DMSO, water and acetic acid for the reaction. The reaction was mechanically stirred at 150 rpm for 36 hours at room temperature and subsequently functionalized with the PS (CMDx) via reaction with EDC/NHS[115] at pH= 4.5 – 5 at 150 rpm of agitation for 36 hours at room temperature. Then, nanoparticles were washed three times with ethanol, dried at 60°C in a vacuum oven and stored at 4°C to be used in experiments.

Preparation of Thermoresponsive Fluorescent monomer (fTFM)

Thermoresponsive fluorescent monomer (TFM) was synthetized using DBD-F following the procedure reported by Uchiyama[75]**.** TFM with a benzofurazan group was obtained by the reaction of DBD-F and 2-(methylamino)-ethanol at room temperature for 30 minutes and then acryloyl chloride was added at the reaction at 60 °C for 12 hours and purified with a column of silica.

Preparation of Free Thermoresponsive Fluorescent Polymer (fTFP)

NIPAM (2.65 mmol) was copolymerized with TFM (0.4 mmol) using MBA (0.324 mmol) as crosslinker, AIBN (0.304 mmol) as initiator agent, and acetone (200ml) as solvent. The solution kept at 60°C for eight hours while stirring at 200 rpm. Later, fTFP was precipitated with diethyl ether (3:1) v/v.

Preparation of TFP coated IO and ICO nanoparticles (IO-TFP and ICO-TFP)

The peptized nanoparticles were functionalized with MPS, in presence of water, ammonium hydroxide, and excess ethanol with an agitation at 150 rpm for 72 hours at room temperature. The resulting nanoparticles were coated with a layer of TFP by free radical polymerization of TFM, NIPAM, MBA as crosslinker and AIBN as initiator agent following the technique reported by Herrera and coworkers[74].

5.2.2 Characterization

The infrared spectra of the nanoparticles were obtained using FT-IR (Bruker IF 66 V/S).The hydrodynamic diameter of the nanoparticles in deionized water at 0.01% w/v was measured through Dynamic Light Scattering (DLS) using a Brookhaven Instruments BI-90Plus Particle Size Analyzer. The size and size distribution of the synthesized magnetic nanoparticles were determined by Transmission Electron Microscopy (TEM) using a Zeiss LEO 922 operating at 200 kV.   For these measurements, the copper grids were immersed in samples of nanoparticles suspended in water, which were then placed on filter paper and dried in a vacuum oven. The mass percentage of inorganic material in the nanoparticles was determined through thermogravimmetric analysis (TGA) using a TGA/DSC1 Thermogravimetric Analyzer from Mettler-Toledo.

The fluorescence intensity of the nanoparticles was measured using an optical fiber probe (PRO-PROBE-BS-Ocean Optics) and the spectra suite program in order to collect the data. A fiber-optic thermometer (LXT-m3300 BioMed Lab Kit-Thermometry Luxtron Corporation) was used to measure temperature. The AC vs. Frequency curves of the nanoparticles were acquired using a Quantum Design MPMS XL-7 SQUID magnetometer. The alternating magnetic field was generated using an RDO Induction Power Supplies HFI 3 kW unit. A three-turn coil was used to generate field amplitudes of [11-45] kA/m and at a frequency of 233 kHz. The coil was cooled using circulating water to approximately 20^0C.

5.2.3 Results and discussion

Figure 16. a) Illustrates the TEM for the different particles used in this study. The size obtained for them were: 16.3 ± 3.2 nm, 14.5 ± 3.3 nm, 14.8 ± 2 nm and 14.9 ± 4 nm for IO-PS, IO-TFP, ICO-PS and ICO-TFP respectively (see **Appendix A7**). The hydrodynamic diameters obtained for IO-PS and ICO-PS in deionized water at 0.1% w/v were 49 ± 3 nm and 50 ± 1nm. While the hydrodynamic diameter in deionized water for IO-TFP and ICO-TFP at 25°C and 40°C (corresponding to T< LCST and T > LCST) were 92 ± 10 nm, 38 ± 5 nm and 106 ± 12.7 nm, 38.66 ± 8 nm. These results are shown in **Figure 16.b**

Figure 16.c) and **d)** shows the hydrodynamic diameter of IO-TFP and ICO-TFP at different temperatures ranging from 20° to 45°C at temperature intervals of 1°C and with stabilization time of 2 minutes before each measurement, indicating the p-NIPAM phase transition around 32°C in both cases.

The different particles were studied by thermogravimetric analysis. TGA data plotted as weight percentage as a function of temperature (**see Appendix A8**) indicated that the mass remaining at the end of the TGA run for ICO-TFP, IO-TFP, IO-PS and ICO-PS were 30.46%, 27.66%, 9.5% and 11.9% respectively.
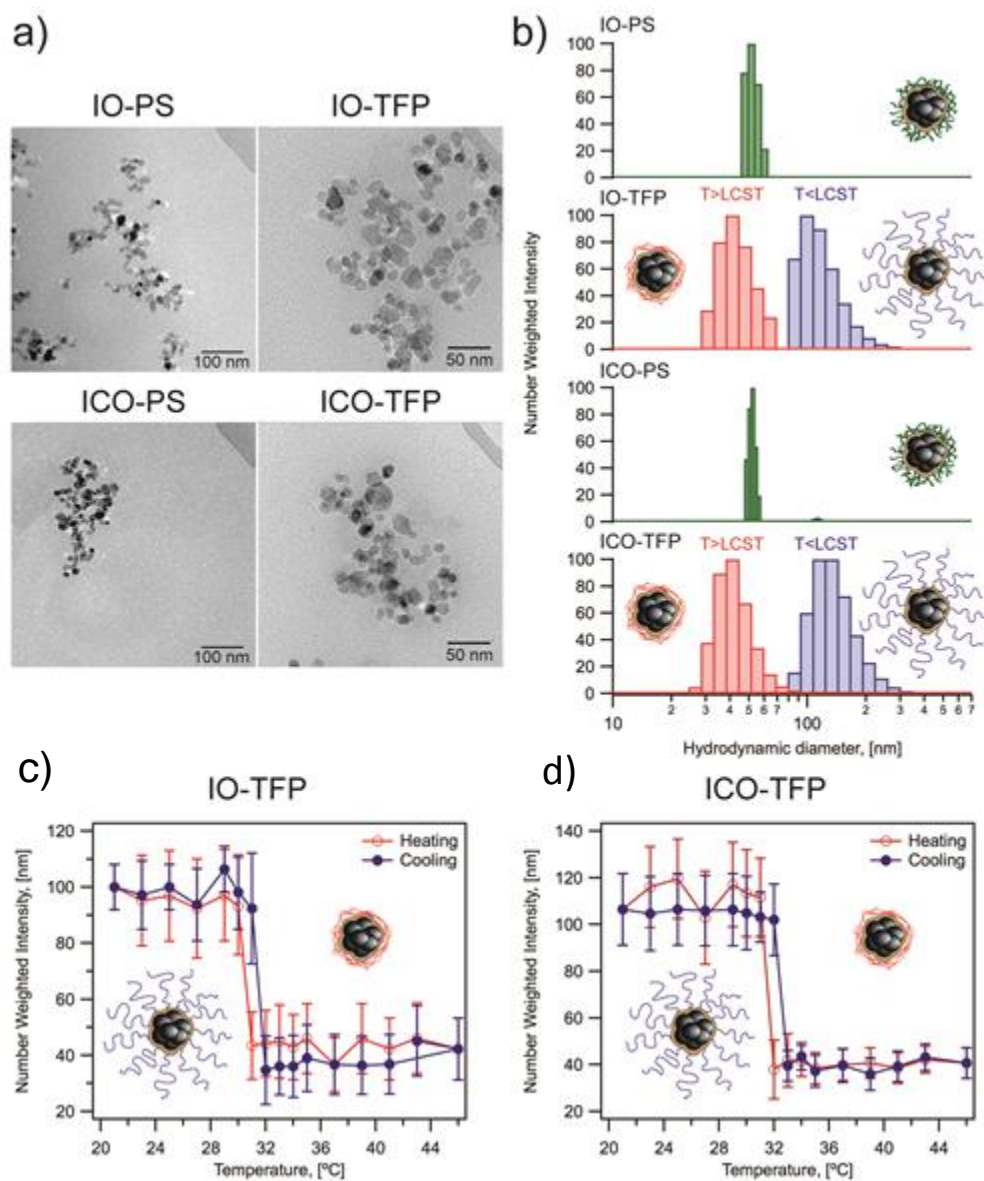
Figure 16.- a) TEM images for the different nanoparticles. b) Hydrodynamic diameter for the different nanoparticles. c) Hydrodynamic diameter for IO-TFP at different temperatures and d) Hydrodynamic diameter for ICO-TFP at different temperatures

AC susceptibility measurements for the different nanoparticles in water-glycerol mixtures at 293 K were made using an AC susceptometer with frequencies between 1000 Hz and 0.1 Hz and drive amplitude of 4 Gauss. **Figure 17** shows in-phase and out-of-phase components of the dynamic susceptibility for IO-PS and ICO-PS nanoparticles. Note that in-phase and out-of-phase AC susceptibility curves for ICO-PS show crossing at the peak of out-of-phase susceptibility curves whereas that IO-PS does not present this behavior. These results indicate that IO-PS and ICO-PS has Neel/Brownian relaxation and Brownian relaxation mechanism respectively.

AC susceptibility measurements were obtained at 280K and 320K for IO-TFP and ICO-TFP nanoparticles in water. For IO-TFP nanoparticles, in-phase and out-of-phase AC susceptibility curves do not cross for either of the two temperatures, however. This fact is observed in the ICO-TFP nanoparticles. Also, a change of the susceptibility measurements with temperature is seen in both cases.
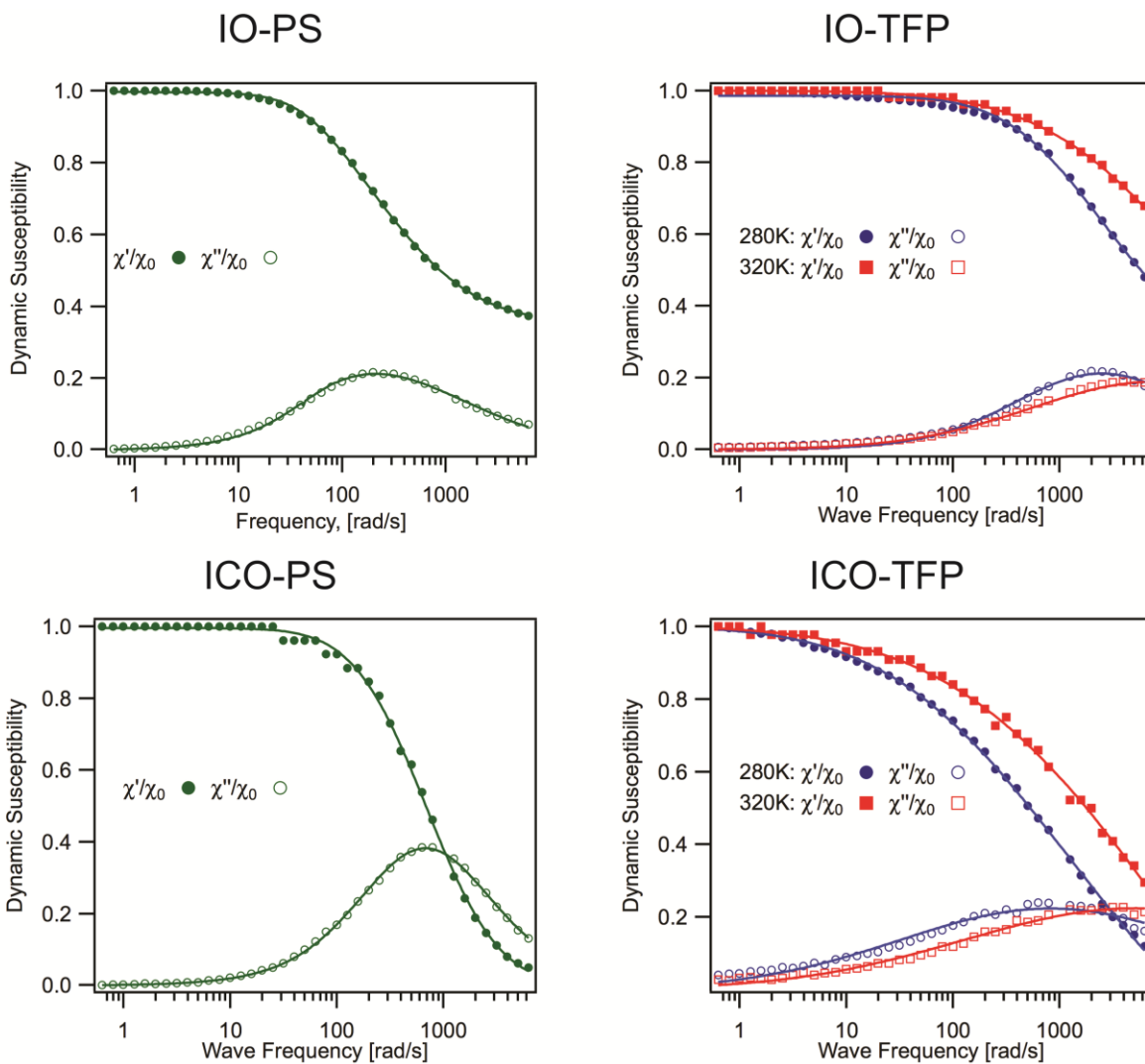
**Figure 17**.- AC vs. Frequency to different nanoparticles IO-PS, IO-TFP, ICO-PS and ICO-TFP

At 280K, the layer of thermoresponsive fluorescent polymer surrounding the magnetite and cobalt-ferrite nanoparticles are in a hydrophilic state, increasing the hydrodynamic diameter and hence their Brownian relaxation time[74]. While, at 320K the thermoresponsive fluorescent polymer chains are contracted decreasing the hydrodynamic diameter.

The hydrodynamic diameter calculated using fits to Debye model yield for each one of the particles are reported in the **Table 7** Comparing the values obtained by means of fit and DLS result for IO-PS and ICO-PS nanoparticles a good agreement is seen.

Table 6.- Calculated hydrodynamic diameter for the different particles using fits of Debye model

Nanoparticle	Hydrodynamic diameter [nm] using Debye model	ln σ	Hydrodynamic diameter [nm] by DLS	ln σ
IO-PS	66-70	0.6	49	0.08
ICO-PS	40	0.3	50	0.045
IO-TFP	89 (280K)	0.5	95 (296K)	2.7
	50 (320K)	0.9	42 (314K)	2.4
ICO-TFP	110-130 (280K)	1	116 (296K)	2.8
	69-98 (320K)	1.2	38 (314K)	1.8

Figure 18.a) shows the fluorescence intensity (left axis) and temperature (right-axis) vs. time. A solution of IO-PS, ICO-PS, IO-TFP and ICO-TFP at 0.5% w/v (magnetic core) in water were exposed to an alternating magnetic field of 38.4 (kA/m) and 233 kHz for a characteristic time. In the beginning, the AMF was off and no changes in temperature or fluorescence were observed. Next the AMF was turned on and a gradual rise in temperature was observed for each particle type. Nevertheless, it was observed that for the IO-TFP the fluorescence intensity increased immediately upon AMF application, even though the medium temperature was still in the range of 22

to 30 °C. No fluorescence increase was perceived for IO-PS + fTFP, ICO-PS + fTFP and ICO-TFP nanoparticles until the medium reached the LCST [118]. **Figure 18.c)** shows the same data as **Figure 18.a)** but plotted fluorescence intensity as a function of temperature in presence and in absence of the magnetic field. The fluorescence remained approximately constant in the temperature range of 30 to 33 °C for IO-PS + fTFP, ICO-PS + fTFP and ICO-TFP nanoparticles while for IO-TFP nanoparticle the fluorescence intensity increased gradually with temperature even when the temperature was below the LCST of pNIPAM.

IO-TFP and IO-PS + fTFP nanoparticles were exposed to 41.78 kA/m and 11.79 kA/m with three different duty cycles at 33, 25 and 20 % illustrated in **Figure 19**. For IO-TFP nanoparticles, at the beginning, no changes in temperature or fluorescence intensity were observed, however during the intervals to 41.78 kA/m and 11.78 kA/m the fluorescence intensity increased immediately at high power and decreased at low power without increase of the medium temperature. For, IO-PS + fTFP nanoparticles these changes were not observed
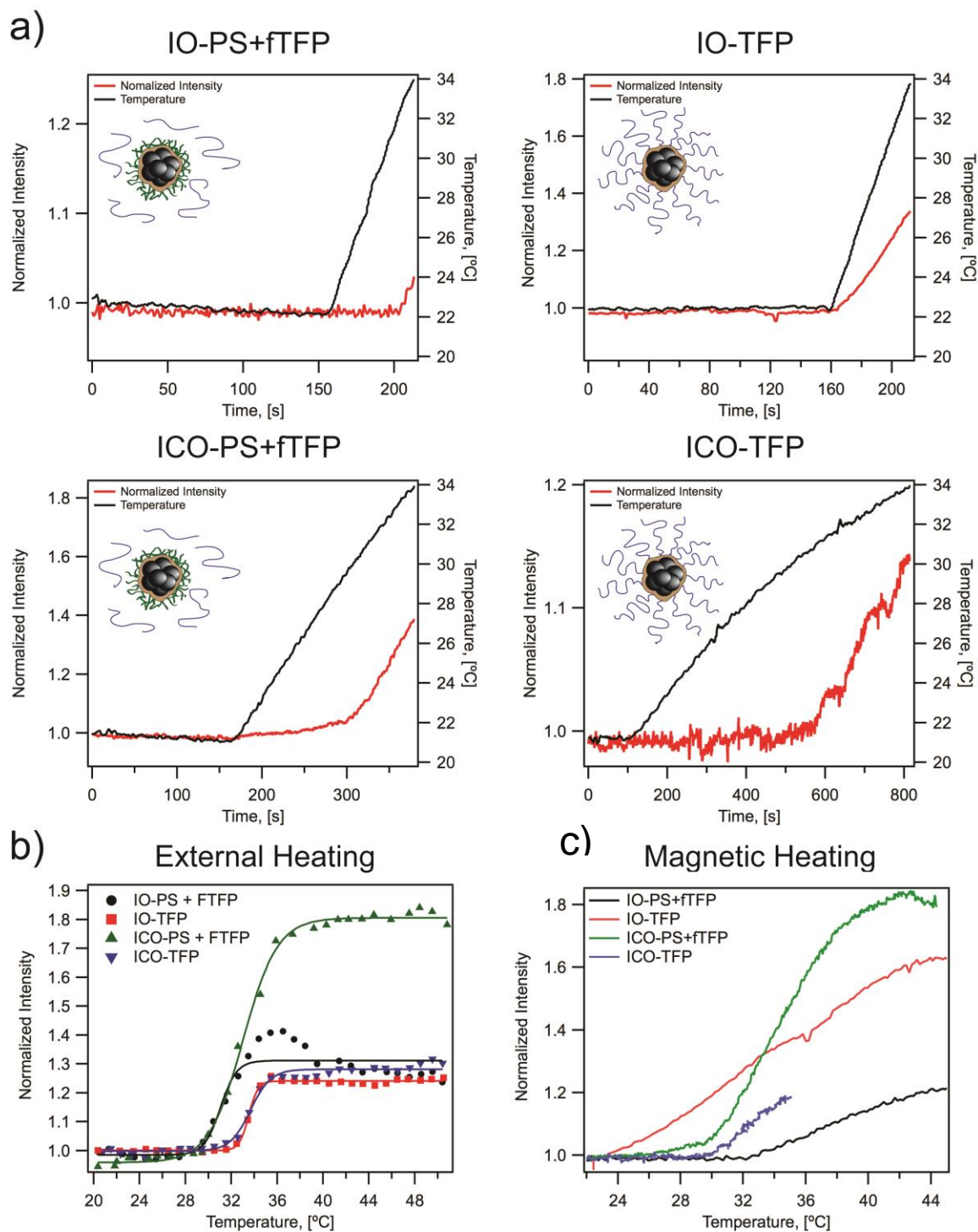
Figure 18.- a) Temperature and fluorescence intensity of the different nanoparticles as a function of time with an AMF 38.4 (kA/m) and to a frequency 233 kHz b) External heating for the different nanoparticles types c) Fluorescence intensity for the different nanoparticles.
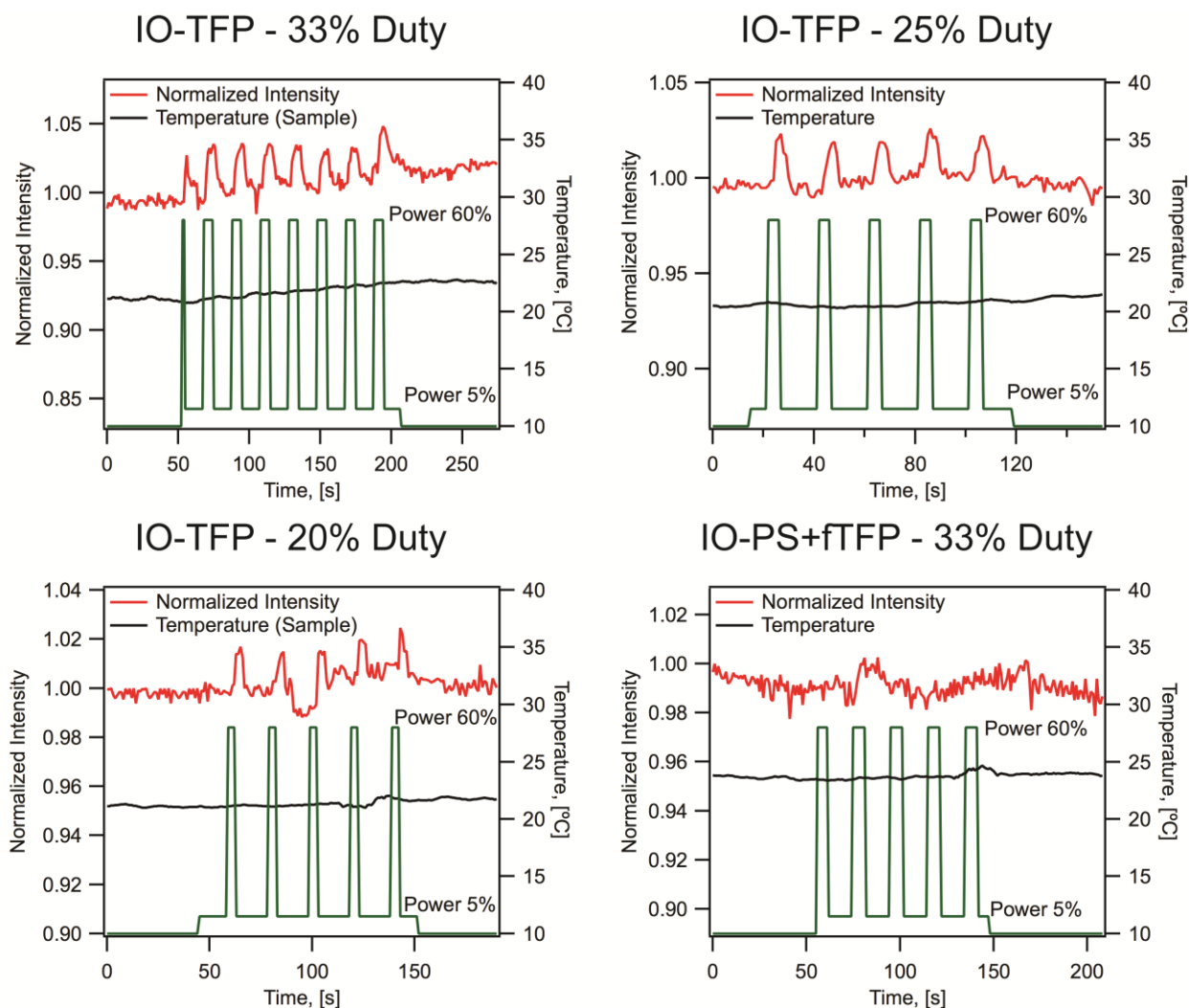
Figure 19.- IO-TFP exposed to 41.78 kA/m and 11.79 kA/m a) Duty cycle 33%, b) Duty cycle 25% and c) Duty cycle 20%. d) IO-PS + FTFP exposed to 41.78 kA/m and 11.79 kA/m to duty cycle 33%.

5.2.4 Conclusion

We have observed indirect evidence of an immediate local thermal effect upon application of the alternating magnetic field of IO-TFP nanoparticles exposed to an AMF compared with IO-PS + fTFP, ICO-PS + fTFP and ICO-TFP nanoparticles.

The fluorescence intensity change of the polymer (TFP) reported the temperature in the immediate vicinity of the nanoparticles, whereas a fiber optic probe reported the temperature of the medium. When external heating was used, the fluorescence intensity for each one of the types nanoparticles was observed to increase at a medium temperature above 32°C, whereas that to IO-TFP nanoparticles, when an AMF was applied, the fluorescence intensity was observed to increase immediately even while the medium temperature was below of the LCST pNIPAM.

The observed change in fluorescence intensity indicated the p-(NIPAM-co-FMA) (TFP) crossed the LCST because the energy dissipation in its vicinity was enough to let that the p-NIPAM chains collapsed and its transition phase were done for nanoparticles with Neel relaxation and TFP chains attached to IO (Iron Oxide) nanoparticles.

6. Scientific Contribution

The application of magnetic nanoparticles as sensor based on the Brownian relaxation mechanism is a novel strategy used to study the interactions and dynamics of network formation in structured materials and it is of great interest in determining mechanical properties of complex fluids in size scale of the nanoparticles. Hence, these magnetic nanoparticles can be used in biomedical field as biosensors for detecting changes in physical properties of biological fluids caused by diseases.

Our scientific contribution in this field was the study of the influence of aging time of the iron-cobalt oleate precursor on the structure, chemical composition, size, and magnetic relaxation of cobalt ferrite nanoparticles synthesized by the thermal decomposition method. This demonstrated that the aging of iron-cobalt oleate complex promoted the formation of the spinel crystal structure which influenced the nanoparticle magnetic properties, resulting in an improvement of the blocking temperature, magnetocrystalline anisotropy constant, and the response to changes in the magnetic field solely by the Brownian relaxation mechanism

Another application of magnetic nanoparticles in biomedical field is related to the study of the local thermal effects on the surface of magnetic nanoparticles in the presence of a magnetic field during the application of Magnetic Fluid Hyperthermia (MFH). Our contribution in this field the discovery and proof that there is an immediate

local thermal effect upon application of the alternating magnetic field (AMF) and that this effect is active only for Neel relaxation mechanism. Nowadays, there is a controversy related with the benefits of the intracellular hyperthermia with respect to extracellular hyperthermia demonstrated by a higher surface temperature of the magnetic nanoparticles with respect to surrounding medium when a magnetic field is applied.

References

[1]   N. Bao, et al., "Formation mechanism and shape control of monodisperse magnetic CoFe2O4 nanocrystals," Chemistry of Materials, vol. 21, pp. 3458-3468, 2009.

[2]   S. Kwon and T. Hyeon, "Colloidal chemical synthesis and formation kinetics of uniformly sized nanocrystals of metal, oxides, and chalcogenides," Accounts of Chemical Research, vol. 41, pp. 1696-1709, 2008.

[3]   M. Polking, et al., "Controlled synthesis and size-dependent polarization domain structure of colloidal germanium telluride nanocrystals," Journal of the American Chemical Society, vol. 133, pp. 2044-2047, 2011.

[4]   B. Srivastava, et al., "Doping Cu in semiconductor nanocrystals: some old and some new physical insights," Journal of the American Chemical Society, vol. 133, pp. 1007-1015, 2011.

[5]   A. Akbarzadeh, et al., "Magnetic nanoparticles: preparation, physical properties, and applications in biomedicine," Nanoscale Research Letters vol. 7, 2012.

[6]   S. Adireddy, et al., "Size-controlled synthesis of quasi-monodisperse transition-metal ferrite nanocrystals in fatty alcohol solutions," Journal of Physics Chemistry C, vol. 113, pp. 20800-20811, 2009.

[7]   G. Baldi, et al., "Cobalt ferrite nanoparticles: the control of the particle size and surface state and their effects on magnetic properties," Journal of Magnetism and Magnetic Materials, vol. 311, pp. 10-16, 2007.

[8]   K. Enpuku, et al., "AC susceptibility measurement of magnetic markers in suspension for liquid phase immunoassay," Journal of Applied Physics, vol. 108, pp. 034701-1-6, 2010.

[9]   A. Habib, et al., "Evaluation of iron-cobalt/ferrite core-shell nanoparticles for cancer thermotherapy," Journal of Applied Physics, vol. 103, pp. 07A313-1-3, 2008.

[10]   X. Yun, et al., "High-magnetic-moment multifunctional nanoparticles for nanomedicine applications," Journal of Magnetism and Magnetic Materials, vol. 311, pp. 131-134, 2007.

[11]   A.-H. Lu, et al., "Magnetic Nanoparticles: Synthesis, Protection, Functionalization, and Application," Chem. Int. Ed, vol. 46, pp. 1222 - 1244, 2007.

[12]   S. P. Gubin, et al., "Magnetic nanoparticles: preparation, structure and properties," Russian Chemical Reviews vol. 74, pp. 489 - 520, 2005.

[13]   M. Faraji, et al., "Magnetic Nanoparticles: Synthesis, Stabilization, Functionalization, Characterization, and Applications," J. Iran. Chem. Soc., vol. 7, pp. 1-37, 2010.

[14]   P. Tartaj, et al., "The preparation of magnetic nanoparticles for applications in biomedicine " J. Phys. D: Appl. Phys, vol. 36, pp. 182-197, 2003.

[15]   G. Reiss and A. Hütten, "Magnetic nanoparticles: Applications beyond data storage " Nature Materials vol. 4, pp. 725 - 726, 2005.

[16]   X. Batlle and A. Labarta, J. Phys. D: Apply. Physvol. 35, 2002.

[17]   J. Gao, et al., "Multifunctional Magnetic Nanoparticles: Design, Synthesis, and Biomedical Applications," Accounts of chemical research, vol. 42, pp. 1097-1107, 2009.

[18]   C. Sun, et al., "Magnetic nanoparticles in MR imaging and drug delivery," Advanced Drug Delivery Reviews, vol. 60, pp. 1252–1265, 2008.

[19]   M. Latorre and C. Rinaldi, "Applications of Magnetic Nanoparticles in Medicine: Magnetic Fluid hyperthermia," Magnetic Fluid Hyperthermia, vol. 28, pp. 227-238, 2009.

[20]   C. C. Berry and A. S. G. Curtis, "Functionalisation of magnetic nanoparticles for applications in biomedicine," J. Phys. D: Appl. Phys, vol. 36, pp. 198–206, 2003.

[21]   M. Hofmann-Amtenbrink, et al., "Superparamagnetic nanoparticles for biomedical applications," in Nanostructured Materials for Biomedical Applications, M. C. Tan, Ed., ed Kerala, India: Transworld Research Network, 2009, pp. 119-149.

[22]   Mahendra Rai, et al., "Biomedical Applications of Nanobiosensors: the State-of-the-Art," J. Braz. Chem. Soc., vol. 23, pp. 14-24,, 2012.

[23]   A. Figuerola, et al., "From iron oxide nanoparticles towards advanced iron-based inorganic materials designed for biomedical applications," Pharmacological Research vol. 62, pp. 126-143, 2010.

[24]   C. S. S. R. Kumar and F. Mohammad, "Magnetic nanomaterials for hyperthermia-based therapy and controlled drug delivery," Advanced Drug Delivery Reviews, vol. 63, pp. 789-808, 2011.

[25]   T. K. Indira and P. K. Lakshmi, "Magnetic Nanoparticles : A Review," Journal of Pharmaceutical Sciences and Nanotechnology, vol. 3, 2010.

[26]   Q. A. Pankhurst, et al., "TOPICAL REVIEW: Applications of magnetic nanoparticles in biomedicine," J. Phys. D: Appl. Phys., vol. 36, pp. R167-R181, 2003.

[27]   T. K. Indira and P. K. Lakshmi, "Magnetic Nanoparticles- Review," International Journal of Pharmaceutical Sciences and Nanotechnology, vol. 3, pp. 1035-1042, 2010.

[28]   Z. Markus, et al., "Magnetic Ferrofluids," in Dekker Encyclopedia of Nanoscience and Nanotechnology, Second Edition - Six Volume Set (Print Version), ed: CRC Press, 2008, pp. 1922-1938.

[29]   V. Calero-DdelC and C. Rinaldi, "Synthesis and magnetic characterization of cobalt-substituted ferrite (CoxFe3-xO4) nanoparticles," Journal of Magnetism and Magnetic Materials, vol. 314, pp. 60-67, 2007.

[30]   Y. Cedeno-Mattei, et al., "Tuning of magnetic properties in cobalt ferrite nanocrystals," Journal of Applied Physics, vol. 103, pp. 07E512-1-3, 2008.

[31]   H. Joshi, et al., "Effects of shape and size of cobalt ferrite nanostructures on their MRI contrast and thermal activation.," Journal of Physics Chemistry C, vol. 113, pp. 17761-17767, 2009.

[32]   K. Kekalo, et al., "Influence of Co amount on the efficiency of energy absorption of Fe-Co ferrite nanoparticles," Journal of Magnetism and Magnetic Materials, vol. 321, pp. 1514-1516, 2009.

[33]   S. H. Chung, et al., "Biological sensors based on brownian relaxation of magnetic nanoparticles," Applied Physics Letters, vol. 85, pp. 2971-2973, 2004.

[34]   J. Nutting, et al., "The effect of particle size distribution on the usage of the ac susceptibility in biosensors," Journal of Applied Physics, vol. 99, pp. 08B319 - 08B319-3, 2006.

[35]   K. Jensen, et al., "An atomic-resolution nanomechanical mass sensor," Nature Nanotechnology, vol. 3, pp. 533-537, 2008.

[36]   M. Li, et al., "Ultra-sensitive NEMS-based cantilevers for sensing, scanned probe and very high-frequency applications," Nature Nanotechnology, vol. 2, pp. 114-120, 2007.

[37]   C. Barrera, et al., "Monitoring gelation using magnetic nanoparticles," Soft Matter, vol. 6, pp. 3662-3668, 2010.

[38]   V. Calero-DdelC, et al., "Quantitative nanoscale viscosity measurements using magnetic nanoparticles and SQUID AC susceptibility measurements," Soft Matter, vol. 7, pp. 4497-4503, 2011.

[39]   A. P. Herrera, et al., "Monitoring colloidal stability of polymer-coated magnetic nanoparticles using AC susceptibility measurements," Journal of Colloid and Interface Science, vol. 342, pp. 540-549, 2010.

[40]   R. E. Rosensweig, Ferrohydrodynamics. Mineola, New York: Dover Publications, Inc, 1985.

[41]   P. C. Fannin, "Investigating magnetic fluids by means of complex susceptibility measurements," Journal of Magnetism and Magnetic Materials, vol. 258, pp. 446-451, 2003.

[42]   P. C. Fannin, "On the high-frequency measurement of the dynamic properties of nano-particle colloids," Journal of Magnetism and Magnetic Materials, vol. 321, pp. 850-853, 2009.

[43]   M. Suto, et al., "Heat dissipation mechanism of magnetite nanoparticles in magnetic fluid hyperthermia " Journal of Magnetism and Magnetic Materials vol. 321, pp. 1493-1496, 2009.

[44]	R. E. Rosensweig, "Heat magnetic fluid with alternating magnetic field," Journal of magnetism and magnetic materials, vol. 252, pp. 370-374, 2002.

[45]	A. K. Gupta and M. Gupta, "Cytotoxicity suppression and cellular uptake enhancement of surface modified magnetic nanoparticles," Biomaterials, vol. 26, pp. 1565-1573, 2005.

[46]	I. Robinson and N. T. K. Thanh, "Recent development for synthsis of magnetic nanoparticles for Biomedical applications," International Journal of Nanoscience, vol. 10, pp. 883-890, 2011.

[47]	C. Schweiger, et al., "Novel magnetic iron oxide nanoparticles coated with poly(ethyleneimine)-g-poly(ethylene glycol) for potential biomedical application: Synthesis, stability, cytotoxicity and MR imaging," International Journal of Pharmaceutics, vol. 408, pp. 130-137, 2011.

[48]	J. Crawford, "Clinical uses of pegylated pharmaceuticals in oncology," Cancer Treatment Reviews, vol. 28, pp. 7-11, 2002.

[49]	A. Ruiz, et al., "Short-chain PEG molecules strongly bound to magnetic nanoparticle for MRI long circulating agents," Acta Biomaterialia, vol. In Press Corrected Proof 2013.

[50]	C. I. Covaliu, et al., "Core–shell hybrid nanomaterials based on CoFe2O4 particles coated with PVP or PEG biopolymers for applications in biomedicine," Powder Technology, vol. In Press, Corrected Proof, 2012.

[51]	C. Barrera, et al., "Colloidal dispersions of monodisperse magnetite nanoparticles modified with poly(ethylene glycol)," Journal of Colloid and Interface Science vol. 329, pp. 107-113, 2009.

[52]	C. Barrera, et al., "Surface modificationofmagnetitenanoparticlesforbiomedicalapplications," Journal of Magnetism and Magnetic Materials vol. 321, pp. 1397-1399, 2009.

[53]	C. Barrera, et al., "Effect of poly(ethylene oxide)-silane graft molecular weight on the colloidal properties of iron oxide nanoparticles for biomedical applications," Journal of Colloid and Interface Science, vol. 377, pp. 40-50, 2012.

[54]	S. García-Jimeno and J. Estelrich, "Ferrofluid based on polyethylene glycol-coated iron oxide nanoparticles: Characterization and properties," Colloids and Surfaces A: Physicochem. Eng. Aspects vol. 420, pp. 74- 81, 2012.

[55]	X. Cao, et al., "Synthesis and Properties of MPEG-Coated Superparamagnetic Magnetite Nanoparticles," Journal of Nanomaterials, vol. 607296, p. 6, 2012.

[56]	J.-B. Qu, et al., "PEG-chitosan-coated iron oxide nanoparticles with high saturated magnetization as carriers of 10-hydroxycamptothecin: Preparation, characterization and cytotoxicity studies," Colloids and Surfaces B: Biointerfaces, vol. 102, pp. 37-44, 2013.

[57]   E. Cheraghipour, et al., "PEG conjugated citrate-capped magnetite nanoparticles for biomedical applications," Journal of Magnetism and Magnetic Materials, vol. 328, pp. 91-95, 2013.

[58]   S. A. Shah, et al., "PEG-coated folic acid-modified superparamagnetic MnFe2O4 nanoparticles for hyperthermia therapy and drug delivery," Materials Chemistry and Physics, vol. 138, pp. 703-708, 2013.

[59]   R. Khatiri, et al., "Immobilization of serum albumin on the synthesized three layers core–shell structures of super-paramagnetic iron oxide nanoparticles," Journal of Industrial and Engineering Chemistry vol. in press, 2013.

[60]   C. Fang, et al., "Fabrication of magnetic nanoparticles with controllable drug loading and release through a simple assembly approach," Journal of Controlled Release vol. 162, pp. 233-241, 2012.

[61]   A. S. A. Lila, et al., "Multiple administration of PEG-coated liposomal oxaliplatin enhances its therapeutic efficacy: A possible mechanism and the potential for clinical application," International Journal of Pharmaceutics, vol. 438, pp. 176- 183, 2012.

[62]   S. A. Shah, et al., "PEG-coated folic acid-modified superparamagnetic MnFe2O4 nanoparticles for hyperthermia therapy and drug delivery," Materials Chemistry and Physics vol. 138, pp. 703-708, 2013.

[63]   A. J. Cole, et al., "Magnetic brain tumor targeting and biodistribution of long-circulating PEG-modified, cross-linked starch-coated iron oxide nanoparticles," Biomaterials, vol. 32, pp. 6291–6301, 2011.

[64]   M.-K. Yoo, et al., "Folate–PEG–superparamagnetic iron oxide nanoparticles for lung cancer imaging," Acta Biomaterialia, vol. 8, pp. 3005-3013, 2012.

[65]   B. Feng, et al., "Synthesis of Fe3O4/APTES/PEG diacid functionalized magnetic nanoparticles for MR imaging," Colloids and Surfaces A: Physicochem. Eng. Aspects vol. 328, pp. 52-59, 2008.

[66]   W. Brullot, et al., "Versatile ferrofluids based on polyethylene glycol coated iron oxide nanoparticles," Journal of Magnetism and Magnetic Materials vol. 324, pp. 1919-1925, 2012.

[67]   X. Qiao, et al., "Magnetorheological Behavior of Polyethyene Glycol-Coated Fe3O4 Ferrofluids," Journal of the Society of Rheology-Japan, vol. 38, pp. 23-30, 2010.

[68]   R. Liu, et al., "Thermoresponsive copolymers: from fundamental studies to applications," Colloid and Polymer Science, vol. 287, pp. 627-643, 2009.

[69]   C.-Y. Chen and C.-T. Chen, "A PNIPAM based fluorescent nanothermometer with ratiometric readout.," Chem.Commun, vol. 47, pp. 994-996, 2011.

[70]   Z. M. O. Rzaev, et al., "Functional copolymers of N-isopropylacrylamide for bioengineering applications.," Prog. Polym Sci, vol. 32, pp. 534-595, 2007.

[71]   L. F. Yan, et al., "Lower critical solution temperature of linear PNIPA obtained from a Yukawa potential of polymer chains," Journal of Applied Polymer Science, vol. 78, pp. 1971-1976, 2000.

[72]   A. Kumara, et al., "Smart polymers: Physical forms and bioengineering applications," Prog. Polym. Sci, vol. 32 pp. 1205-1237, 2007.

[73]   X. B. Bing, et al., "Preparation of thermosensitive magnetic particles by dispersion polymerization.," Reactive and Functional Polymers, vol. 38, pp. 11-15, 1999.

[74]   A. P. Herrera, et al., "Multifunctional magnetite nanoparticles coated with fluorescent thermo-responsive polymeric shells," J. Mater. Chem., vol. 18, pp. 855-858, 2008.

[75]   S. Uchiyama, et al., "Fluorescent Molecular Thermometers Based on Polymers Showing Temperature-Induced Phase Transitions and Labeled with Polarity-Responsive Benzofurazans," Anal. Chem, vol. 75, pp. 5926-5935, 2003.

[76]   S. Uchiyama, et al., "Fluorescence characteristics of six 4,7-disubstituted benzofurazan compounds: an experimental and semi-empirical MO study," J. Chem. Soc., Perkin Trans. 2, , pp. 2525-2532, 1999.

[77]   H. B. Na, et al., "Inorganic Nanoparticles for MRI Contrast Agents," Adv. Mater, vol. 21, pp. 2133–2148, 2009.

[78]   H. Yim, et al., "MRI Contrast Agent-BasedMultifunctionalMaterials: Diagnosis and Therapy- Review " Journal of Nanomaterials, vol. 747196, 2011.

[79]   F. Song, et al., "Fabrication of novel thermo-responsive electrospun nanofibrous mats and their application in bioseparation," European Polymer Journal, vol. 47, pp. 1885–1892, 2011.

[80]   H. Hejase, et al., "MnZnFe nanoparticlesforself-controlledmagetichyperthermia," Journal of Magnetism and Magnetic Materials, vol. 324, pp. 3620-3628, 2012.

[81]   S. Yu, et al., "Magnetic and pH-sensitive nanoparticles for antitumor drug delivery," Colloids and Surfaces B: Biointerfaces, vol. 103, pp. 15-22, 2013.

[82]   O. Veiseh, et al., "Design and fabrication of magnetic nanoparticles for targeted drug delivery and imaging," Advanced Drug Delivery Reviews vol. 62, pp. 284-304, 2010.

[83]   L. M. Shayna, et al., "Magnetically Responsive Nanoparticles for DrugDelivery Applications Using Low MagneticField Strengths," IEEE Transactions on Nanobioscience vol. 8, pp. 33-42, 2009.

[84]   J.-P. Fortin, et al., "Intracellular heating of living cells through Neel relaxation of magnetic nanoparticles," Eur Biophys J vol. 37, pp. 223-228, 2008.

[85] K. M. Krishnan, "Biomedical Nanomagnetics: A Spin Through Possibilities in Imaging, Diagnostics, and Therapy," IEEE Transactions on magnetic vol. 46, pp. 2523-2558, 2010.

[86] C. S. S. R. Kumar and F. Mohammad, "Magnetic nanomaterials for hyperthermia-based therapy and controlled drug delivery," Advanced Drug Delivery Reviews vol. 63, pp. 789–808, 2011.

[87] V. L. Calero-DdelC, et al., "Quantitative nanoscale viscosity measurements using magnetic nanoparticles and SQUID AC susceptibility measurements," Soft Matter, vol. 7, pp. 4497-4503, 2011.

[88] V. L. Calero-DdelC, et al., "Magnetic Fluid and Nanoparticle Based Sensors," in Encyclopedia of Sensors. vol. X, C. A. Grimes, et al., Eds., ed, 2005, pp. 1-13.

[89] C. J. Behrend, et al., "Microrheology with modulated optical nanoprobes (MOONs)," Journal of Magnetism and Magnetic Materials, vol. 293, pp. 663-670, 2005.

[90] J. N. Anker, et al., "Magnetically-modulated optical nanoprobes (MagMOONs) and systems," Journal of Magnetism and Magnetic Materials vol. 293, pp. 655-662, 2005.

[91] C. Wilhelm and F. Gazeau, "Magnetic nanoparticles: Internal probes and heaters within living cells " Journal of Magnetism and Magnetic Materials vol. 321, pp. 671-674, 2009.

[92] J. Connolly and T. G. S. Pierre, "Proposed biosensors based on time-dependent properties of magnetic fluids," Journal of Magnetism and Magnetic Materials, vol. 225, pp. 156-160, 2001.

[93] V. K. Varadan, et al., "Nanomedicine design and applications of magnetic nanomaterials, nanosensors and nanosystems": Wiley, 2008.

[94] S. H. Chung, et al., "Biological sensors based on Brownian relaxation of magnetic nanoparticles," Applied Physics Letters, vol. 85, pp. 2971-2972, 2004.

[95] A. Fornara, et al., "Tailored Magnetic Nanoparticles for Direct and Sensitive Detection of Biomolecules in Biological Samples," Nano Lett., vol. 8, pp. 3423-3428, 2008.

[96] A. P. Astalan, et al., "Biomolecular reactions studied using changes in Brownian rotation dynamics of magnetic particles," Biosensors and Bioelectronics vol. 19, pp. 945-951, 2004.

[97] N. Bao, et al., "Formation mechanism and shape control of monodisperse magnetic CoFe2O4 nanocrystals," Chemistry of Materials, vol. 21, pp. 3458-3468,, 2009.

[98] N. Bao, et al., "A facile thermolysis route to monodisperse ferrite nanocrystals," Journal of the American Chemical Society, vol. 29, pp. 12374-12375, 2007.

[99] N. Bao, et al., "A facile thermolysis route to monodisperse ferrite nanocrystals," Journal of the American Chemical Society, vol. 129, pp. 12374-12375, 2007.

[100]   K. Park, et al., "Ultra large-scale synthesis of monodisperse nanocrystals," Nature Materials, vol. 3, pp. 891-895, 2004.

[101]   D. G. Rancourt and J. Y. Ping, "Voigt-based methods for arbitrary-shape static hyperfine parameter distributions in Mössbauer Spectroscopy," Nuclear Instruments and Methods in Physics Research Section B., vol. 58, pp. 85-97, 1991.

[102]   V. Calero-DdelC and C. Rinaldi, "Effect of sample concentration on the determination of the anisotropy constant of magnetic nanoparticles," IEEE Transactions on Magnetics, vol. 46, pp. 852-859, 2010.

[103]   R. Chantrell, et al., "Measurements of particle size distribution parameters in ferrofluids," IEEE Transactions on Magnetics, vol. 14, pp. 975-977, 1978.

[104]   J. Popplewell and L. Sakhnini, "The dependence of the physical and magnetic properties of magnetic fluids on particle size," Journal of Magnetism and Magnetic Materials, vol. 149, pp. 72-78, 1995.

[105]   B. Cullity and S. Stock, Elements of X-ray diffraction, Third ed. New Jersey: Prentice Hall, Inc., 2001.

[106]   X. Li, et al., "Preparation and characterization of superparamagnetic nanocrystalline cobalt ferrite materials," Journal of Materials Science Letters, vol. 21, pp. 1881-1883, 2002.

[107]   G. Glaspell, et al., "Formation of cobalt nitrate hydrate, cobalt oxide, and cobalt nanoparticles using laser vaporization controlled condensation," Journal of Physical Chemistry B, vol. 108, pp. 9604-9607, 2004.

[108]   C. Cannas, et al., "CoFe2O4 and CoFe2O4/SiO2 core/shell nanoparticles: Magnetic and spectroscopy study.," Chemistry of Materials, vol. 22, pp. 3353-3361, 2010.

[109]   P. Jeppson, et al., "Cobalt ferrite nanoparticles: Achieving the superparamagnetic limit by chemical reduction.," Journal of Applied Physics, vol. 100, pp. 114324-1-6, 2006.

[110]   J. Nogues, et al., "Shell-driven magnetic stability in core-shell nanoparticles," Physical Review Letters, vol. 97, pp. 157203-1-4, 2006.

[111]   S. Odenbach, Magnetoviscous effects in ferrofluids. Germany: Springer, 2002.

[112]   V. Calero DdelC, et al., "Magnetic fluid and magnetic nanoparticle based sensors," in Encyclopedia of Sensors. vol. 5, C. A. Grimes, et al., Eds., ed: American Scientific Publishers, 2006, pp. 389-401.

[113]   P. C. Fannin, et al., "New technique for measuring the complex susceptibility of ferrofluids," Journal of Physics E-Scientific Instruments, vol. 19, pp. 238-239, 1986.

[114]   H. L. Rodríguez-Luccioni, et al., "Enhanced reduction in cell viability by hyperthermia induced by magnetic nanoparticles," International Journal of Nanomedicine, vol. 6 pp. 373-380, 2011.

[115]   M. Creixell, et al., "EGFR-targeted magnetic nanoparticle heaters can kill cancer cells without a perceptible temperature rise," ACS NANO, vol. 5, pp. 7124-7129, 2011.

[116]   Y. Rabin, "Is intracellular hyperthermia superior to extracellular hyperthermia in thermal sense?," Int. J. Hyperthermia 18, vol. 18, pp. 194-202, 2002.

[117]   H. Huang, et al., "Remote control of ion channels and neurons through magnetic-field heating of nanoparticles," Nature Nanotechnology, vol. 5, pp. 602-606, 2010.

[118]   L. Polo-Corrales and C. Rinaldi, "Monitoring iron oxide nanoparticle surface temperature in an alternating magnetic field using thermoresponsive fluorescent polymers," Journal of Applied physics, vol. 111, 07B334, 2012.

[119]   D. Needham and M. W. Dewhirst, "The development and testing of a new temperature-sensitive drug delivery system for the treatment of solid tumors.," Adv. Drug Delivery Rev, vol. 53, pp. 285-305, 2001.

[120]   M. B. Yatvin, et al., "Design of liposomes for enhanced local release of drugs by hyperthermia," Science, vol. 202, pp. 1290-1293, 1978.

[121]   E. Amstad and E. Reimhult, "Nanoparticle actuated hollow drug delivery vehicles," Nanomedicine, vol. 7, pp. 145-164, 2012.

[122]   J. Chomoucka, et al., "Magnetic nanoparticles and targeted drug delivering," Pharmacological Research, vol. 62, pp. 144-149, 2010.

[123]   T. Hoare, et al., "Magnetically Triggered Nanocomposite Membranes: A Versatile Platform for Triggered Drug Release," Nano Lett., vol. 1 pp. 1395-1400, 2011.

[124]   T.-Y. Liu, et al., "Biomedical nanoparticle carriers with combined thermal and magnetic responses," Nano Today vol. 4, pp. 52-65, 2009.

[125]   E. Amstad, et al., "Triggered Release from Liposomes through Magnetic Actuation of Iron Oxide Nanoparticle Containing Membranes," Nano Lett., vol. 11, pp. 1664-1670, 2011.

[126]   B. D. Mistry, "A Handbook of Spectroscopic Data CHEMISTRY(UV, JR, PMR, JJCNMR and Mass Spectroscopy," Edition 2009 Va/sad - (Gujarat) Oxford.

[127]   A. P. Herrera, et al., "Monitoring colloidal stability of polymer - coated magnetic nanoparticles using AC susceptibility measurements," Journal of colloid and Interface science, vol. 342, pp. 540-549, 2010.

[128]   Y. Cedeno-Mattei, et al., "Tunning of magnetic properties in cobalt ferrite nanoparticles," Journal of Applied Physics, vol. 103, pp. 07E512-1- 07E512-3, 2008.

[129]   A. J. Gomes, et al., "Synthesis of Core-Shell Ferrite Nanoparticles for Ferrofluids: Chemical and Magnetic Analysis," J. Phys. Chem. C vol. 112, pp. 6220-6227, 2008.

Appendix
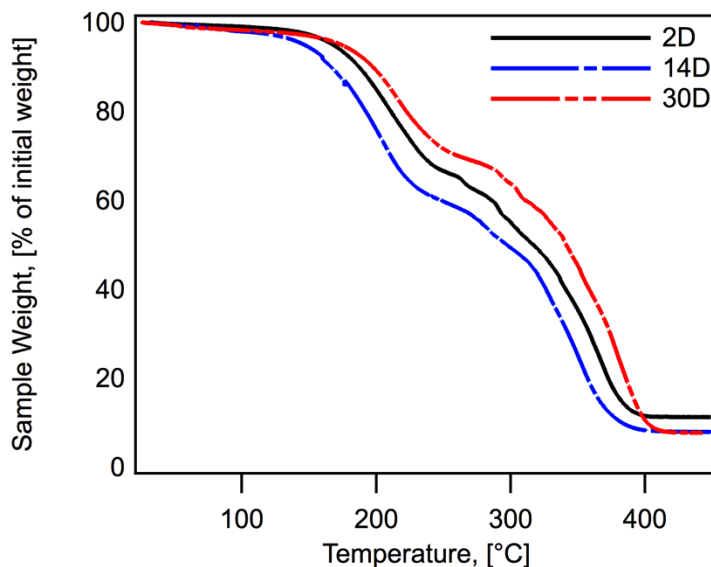
A1. TGA measurements of the iron-cobalt oleate aged for 2, 14, and 30 days. The weight loss percentage was recorded with a heating rate of 3.5 °C/min using air at 60 ml/min.
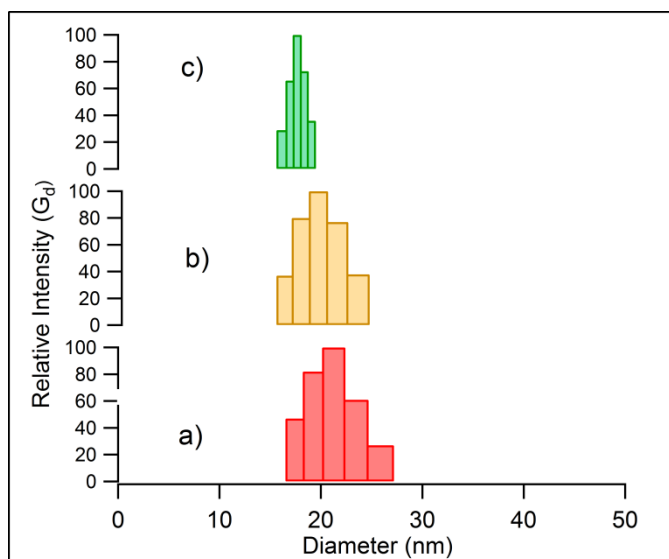
A2. Volume weighted size distributions according to DLS for cobalt ferrite nanoparticles suspended in hexane and filtered with 0.1 μm PTFE filter syringes. Graphs (a), (b), and (c) show nanoparticles synthesized using iron-cobalt oleate aged at room temperature for 2, 14, and 30 days, respectively.
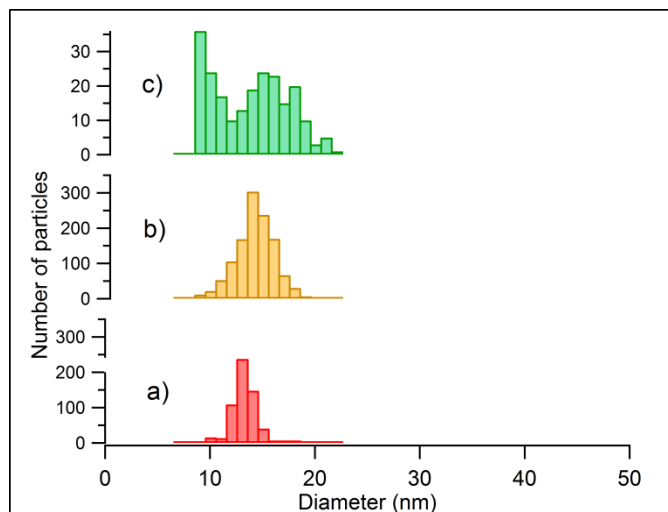
A3. TEM histograms for the size distribution of cobalt ferrite nanoparticles synthesized by the thermal decomposition method using iron-cobalt oleate aged at room temperature for a) 2 days, b) 14 days, and c) 30 days.
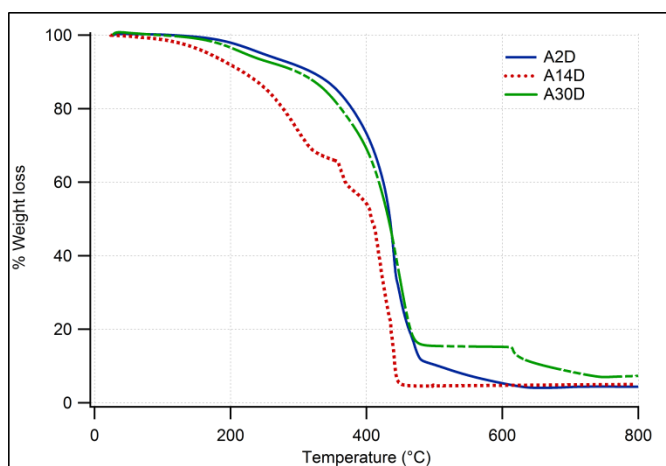

A4. TGA measurement of cobalt ferrite nanoparticles synthesized by the thermal decomposition method after using iron-cobalt oleate aged for 2 days (sample 2D), 14 days (sample 14D), and 30 days (sample 30D). Synthesized nanoparticles were washed three times with acetone (1:3) at 8000 rpm for 30 min. The weight loss percentage was recorded in the temperature range of 25 to 800 °C with a heating rate of 10 °C/min using air at 60 ml/min.

After weight loss normalization, sample composition was estimated by assuming the remnant mass corresponds to the inorganic cores of the magnetic nanoparticles

| Sample	Inorganic %
2D	4.0
14D	5.0
30D	7.3
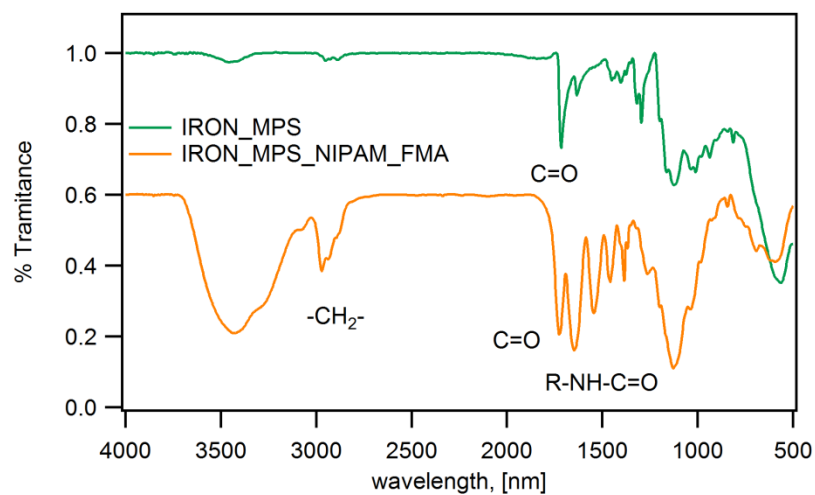
A5. Infrared spectra for Iron_MPS and Iron_NIPAM_FMA
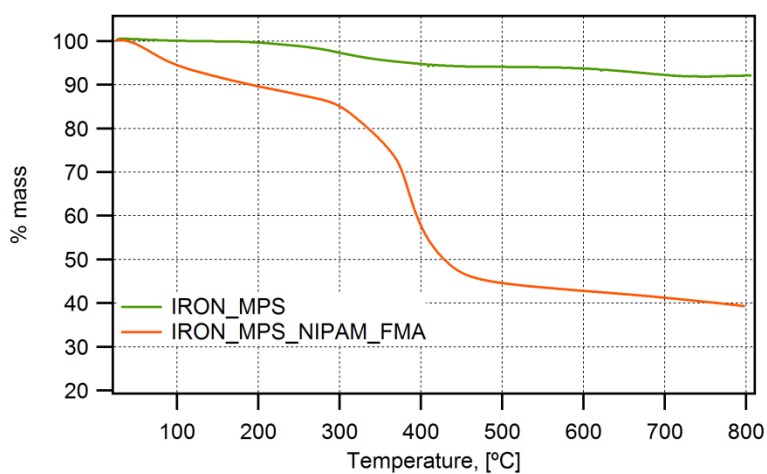
A6. TGA curves of the MPS coated magnetite nanoparticles and p(NIPAM-co-FMA) coated IO nanoparticles
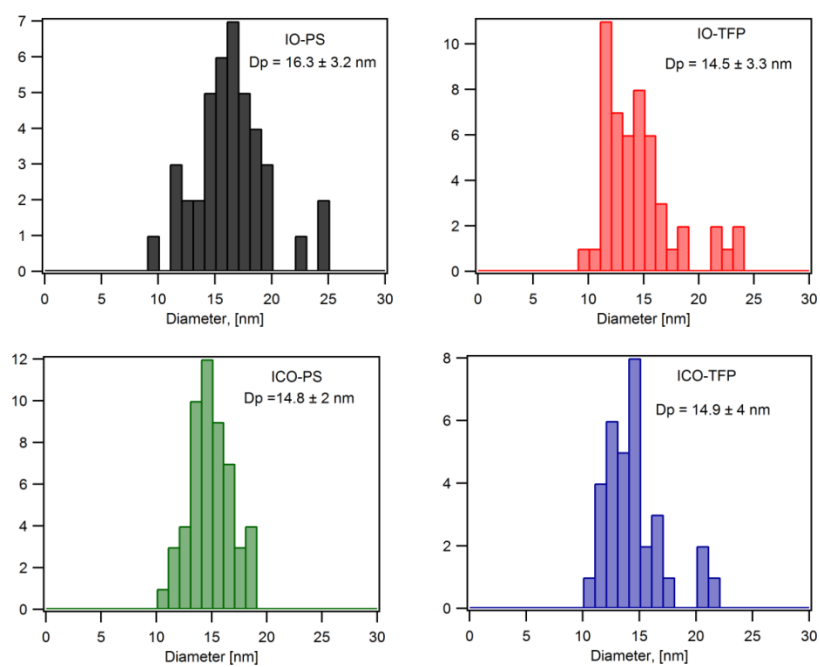
A7. Size distribution of the different nanoparticles by TEM
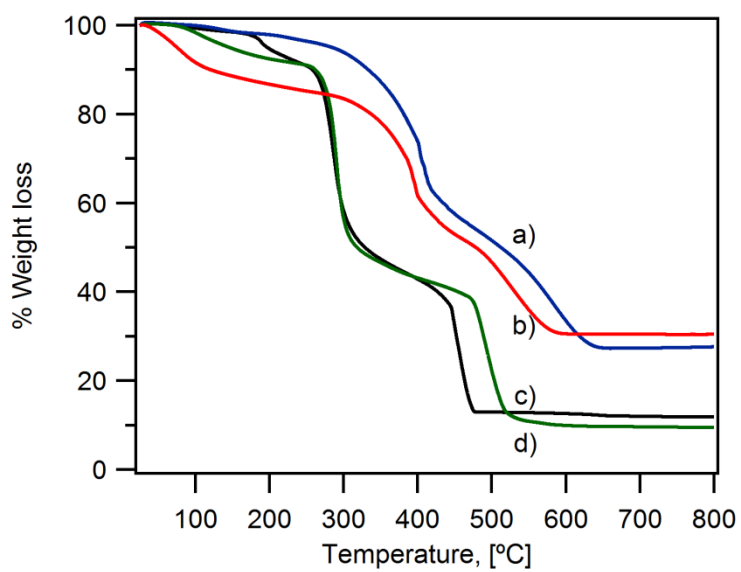
A8. Thermogravimetric analysis of a) ICO-TFP, b) IO-TFP, c) IO-PS and d) ICO-PS